AFRL-AFOSR-VA-TR-2022-0058

Robust Coordination Strategies for Heterogeneous UAS in Limited Communication Environments

Hovakimyan, Naira
UNIVERSITY OF ILLINOIS
352 HENRY ADMINISTRATION BLDG
URBANA, IL, 61801
USA

12/06/2021
Final Technical Report

REPORT DOCUMENTATION PAGE		Form Approved OMB No. 0704-0188

The public reporting burden for this collection of information is estimated to average 1 hour per response, including the time for reviewing instructions, searching existing data sources, gathering and maintaining the data needed, and completing and reviewing the collection of information. Send comments regarding this burden estimate or any other aspect of this collection of information, including suggestions for reducing the burden, to Department of Defense, Washington Headquarters Services, Directorate for Information Operations and Reports (0704-0188), 1215 Jefferson Davis Highway, Suite 1204, Arlington, VA 22202-4302. Respondents should be aware that notwithstanding any other provision of law, no person shall be subject to any penalty for failing to comply with a collection of information if it does not display a currently valid OMB control number.
PLEASE DO NOT RETURN YOUR FORM TO THE ABOVE ADDRESS.

1. REPORT DATE (DD-MM-YYYY) 06-12-2021	2. REPORT TYPE Final	3. DATES COVERED (From - To) 15 Jun 2018 - 14 Jun 2021

4. TITLE AND SUBTITLE	5a. CONTRACT NUMBER
Robust Coordination Strategies for Heterogeneous UAS in Limited Communication Environments	
	5b. GRANT NUMBER FA9550-18-1-0269
	5c. PROGRAM ELEMENT NUMBER 61102F

6. AUTHOR(S)	5d. PROJECT NUMBER
Naira Hovakimyan	
	5e. TASK NUMBER
	5f. WORK UNIT NUMBER

7. PERFORMING ORGANIZATION NAME(S) AND ADDRESS(ES)	8. PERFORMING ORGANIZATION REPORT NUMBER
UNIVERSITY OF ILLINOIS 352 HENRY ADMINISTRATION BLDG URBANA, IL 61801 USA	

9. SPONSORING/MONITORING AGENCY NAME(S) AND ADDRESS(ES)	10. SPONSOR/MONITOR'S ACRONYM(S) AFRL/AFOSR RTA2
AF Office of Scientific Research 875 N. Randolph St. Room 3112 Arlington, VA 22203	
	11. SPONSOR/MONITOR'S REPORT NUMBER(S) AFRL-AFOSR-VA-TR-2022-0058

12. DISTRIBUTION/AVAILABILITY STATEMENT
A Distribution Unlimited: PB Public Release

13. SUPPLEMENTARY NOTES

14. ABSTRACT
During the last three years, we further developed the time-critical cooperative control framework ,initiated under our prior AFOSR grants, to enable novel distributed trajectory-planning and online coordination capabilities for a fleet of cooperating vehicles that communicate over a lossy wireless network. In the field of trajectory planning, the main advances of this research include a distributed algorithm that balances the trajectory-planning workload among all agents in the fleet. The resulting algorithms combine tools from non-linear optimization and distributed programming methods, and leverage the polynomial structure of the trajectories and differential flatness properties of the system dynamics to compute the entire subdifferential analytically. Hence, reducing the computational cost as compared to existing bundle methods. Regarding time-critical coordination, the temporal specification and coordination capabilities of the framework have broadened significantly to accommodate the diversity of constraints required in realistic missions of interest to AFOSR. The distributed time-critical coordination law lets the vehicles adjust their speed in real time to meet the desired temporal and coordination constraints even in the presence of external disturbances. This research introduced a new classification of these constraints that has lead to unprecedented levels of flexibility and adaptability. Moreover, tools from Lyapunov stability, switched systems, and algebraic graph theory were leveraged to derive transient and steady-state performance bounds for some of the new time-critical coordination strategies.
We also initiated new directions of research over the last two years on certified trajectory tracking for nonlinear and uncertain systems on a single-agent level. The certificates are amenable to incorporation within the results as mentioned earlier. Leveraging the L1 architecture, the work in [1] developed a new architecture for the safe incorporation of machine learning in the form of Bayesian Gaussian process regression within robust adaptive control. A major issue for nonlinear control is the synthesis of control certificates which enable the synthesis of feedback laws. Departing from difficult to synthesize Lyapunov functions for nonlinear systems, the work in [2] developed a new direction of using control contraction metric based control with L1 adaptation. The main advantage of this work is the quantification of tubes around any desired trajectory, which is a highly desirable feature for systems attempting to track trajectories in the presence of uncertainties. The work in [3] further developed on contraction L1 in [2] by incorporating Gaussian process learning leading to an improvement in both optimality and performance while guaranteeing persistent safety. The robustification of reinforcement learning policies using L1 control was demonstrated in [4]. The work in [5] shows how barrier function-based control can be made robust to uncertainties. On the level of multi-agent systems, the work in [6] and [7] presents efficient distributed algorithms for stochastic agents aiming to optimize global cost-functions using only local observations. The work in [8] investigates the compositionality of control laws for teams of stochastic agents. These new directions of research were further expanded in our renewal proposal for AFOSR,
and hence we will not summarize those preliminary results in this final report.

15. SUBJECT TERMS

16. SECURITY CLASSIFICATION OF:			17. LIMITATION OF ABSTRACT	18. NUMBER OF PAGES	19a. NAME OF RESPONSIBLE PERSON FREDERICK LEVE
a. REPORT	b. ABSTRACT	c. THIS PAGE			
U	U	U	UU	26	19b. TELEPHONE NUMBER *(Include area code)* 696-9730

Standard Form 298 (Rev.8/98)
Prescribed by ANSI Std. Z39.18

Robust Coordination Strategies for Heterogeneous UAS in Limited Communication Environments

Final report for grant FA9550-18-1-0269

Naira Hovakimyan

Mechanical Science and Engineering Department,
University of Illinois at Urbana-Champaign

Abstract

During the last three years, we further developed the time-critical cooperative control framework, initiated under our prior AFOSR grants, to enable novel distributed trajectory-planning and online coordination capabilities for a fleet of cooperating vehicles that communicate over a lossy wireless network. In the field of trajectory planning, the main advances of this research include a distributed algorithm that balances the trajectory-planning workload among all agents in the fleet. The resulting algorithms combine tools from non-linear optimization and distributed programming methods, and leverage the polynomial structure of the trajectories and differential flatness properties of the system dynamics to compute the entire subdifferential analytically. Hence, reducing the computational cost as compared to existing bundle methods. Regarding time-critical coordination, the temporal specification and coordination capabilities of the framework have broadened significantly to accommodate the diversity of constraints required in realistic missions of interest to AFOSR. The distributed time-critical coordination law lets the vehicles adjust their speed in real time to meet the desired temporal and coordination constraints even in the presence of external disturbances. This research introduced a new classification of these constraints that has lead to unprecedented levels of flexibility and adaptability. Moreover, tools from Lyapunov stability, switched systems, and algebraic graph theory were leveraged to derive transient and steady-state performance bounds for some of the new time-critical coordination strategies.

We also initiated new directions of research over the last two years on certified trajectory tracking for nonlinear and uncertain systems on a single-agent level. The certificates are amenable to incorporation within the results as mentioned earlier. Leveraging the $\mathcal{L}_1$ architecture, the work in [1] developed a new architecture for the safe incorporation of machine learning in the form of Bayesian Gaussian process regression within robust adaptive control. A major issue for nonlinear control is the synthesis of control certificates which enable the synthesis of feedback laws. Departing from difficult to synthesize Lyapunov functions for nonlinear systems, the work in [2] developed a new direction of using control contraction metric based control with $\mathcal{L}_1$ adaptation. The main advantage of this work is the quantification of tubes around *any* desired trajectory, which is a highly desirable feature for systems attempting to track trajectories in the presence of uncertainties. The work in [3] further developed on contraction $\mathcal{L}_1$ in [2] by incorporating Gaussian process learning leading to an improvement in both optimality and performance while guaranteeing *persistent* safety. The robustification of reinforcement learning policies using $\mathcal{L}_1$ control was demonstrated in [4]. The work in [5] shows how barrier function-based control can be made robust to uncertainties. On the level of multi-agent systems, the work in [6] and [7] presents efficient distributed algorithms for stochastic agents aiming to optimize global cost-functions using only local observations. The work in [8] investigates the compositionality of control laws for teams of stochastic agents. These new directions of research were further expanded in our renewal proposal for AFOSR, and hence we will not summarize those preliminary results in this final report.

I. INTRODUCTION

The research developed for this grant addressed theoretical topics of practical importance in the field of autonomy for multi-agent systems. This effort aimed to expand the capabilities of the system architecture [9], [10], depicted in Figure 1, to bridge the gap between theory and application, expand the flexibility of the framework to a larger class of missions, and adapt to the growing complexity demanded of cooperating agents [11], [12]. This framework is based on two fundamental ideas. First, decoupling space and time to ensure vehicles can track their path regardless of their speed profile, as long as it is physically feasible [13]. Second, the compartmentalization of each task within the framework — trajectory-generation, path-following, time coordination, and vehicle stabilization — so that different algorithms and technologies can be swapped with ease [13]. This compartmentalization and space-time decoupling allows the higher-level algorithms, such as time-coordination, to abstract away from the vehicle dynamics, which allows for the design of more elaborate time-coordination laws that adapt to the demanding complexity with known guarantees [14], [15]. In particular, this effort sought to advance the state-of-the-art in motion control of distributed systems through two different thrusts: the interaction with switched dynamics that arise when attempting to implement certain types of temporal constraints, and the propagation of perturbations through networked systems with this switching dynamics. The next section contains a brief summary of the problem formulation.

II. PROBLEM FORMULATION

A. Path Following

As described in [9], [16], the key idea of the path-following algorithm is to use the control effectors of the UAS to follow a *virtual target* that slides along the path. To this effect, a moving frame is attached to the virtual target, and a generalized error vector that characterizes the distance between this moving coordinate system and a frame attached to the UAS is defined, as shown in Figure 13. To control the movement of the virtual target along the path, we introduce a *virtual time* $\xi_i(t)$ that defines the position of the virtual target

$$\boldsymbol{p}_{\boldsymbol{\tau},\boldsymbol{i}}(t) := \boldsymbol{p}_{\boldsymbol{d},\boldsymbol{i}}(\xi_i(t)), \tag{1}$$

and define the position error

$$\boldsymbol{e}_{\boldsymbol{p},\boldsymbol{i}}(t) := \boldsymbol{p}_{\boldsymbol{i}}(t) - \boldsymbol{p}_{\boldsymbol{\tau},\boldsymbol{i}}(t),$$

where $\boldsymbol{p}_{\boldsymbol{i}}(t)$ denotes the actual position of the ith vehicle at time t. Then, the dynamics of the position error are

$$\dot{\boldsymbol{e}}_{\boldsymbol{p},\boldsymbol{i}}(t) = \boldsymbol{v}_{\boldsymbol{i}}(t) - \boldsymbol{v}_{\boldsymbol{\tau},\boldsymbol{i}}(t), \tag{2}$$
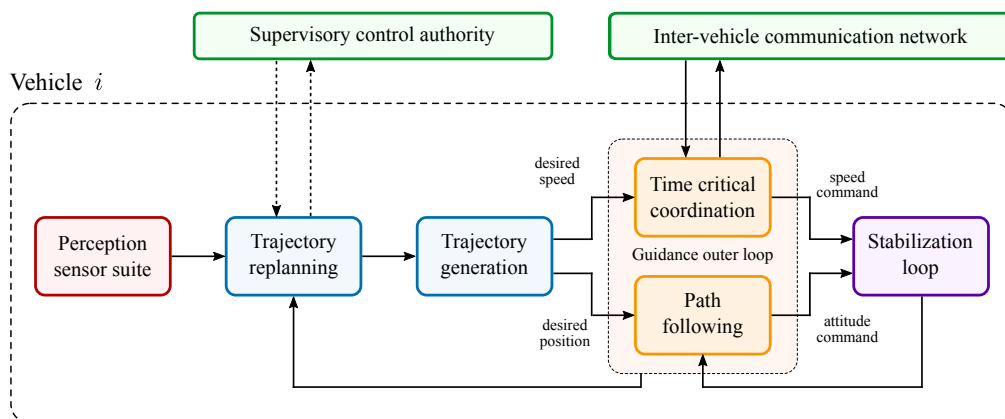

Fig. 1: Architecture of the time-critical coordination framework.

where $v_i(t)$ is the velocity vector of the UAS, and $v_{\mathcal{T},i}(t)$ is the velocity vector of the virtual target, as depicted in Figure 13. The velocity of the virtual target can be expressed in terms of the desired velocity

$$v_{\mathcal{T},i}(t) = \dot{\xi}_i(t)\, v_{d,i}(\xi_i(t)). \tag{3}$$

Now, define the velocity-tracking error

$$e_{v,i}(t) = v_i(t) - v_{cmd,i}(t),$$

where $v_{cmd,i}(t)$ is the velocity command generated by the guidance outer loop, and choose the following control law for the velocity command:

$$v_{cmd,i}(t) := v_{\mathcal{T},i}(t) - k_{PF,i}\, e_{p,i}(t), \tag{4}$$

where $k_{PF,i} > 0$ is a control gain. Note that vehicles within the cooperative fleet can implement different gains $k_{PF,i}$. This offers the possibility of fine tuning this algorithm for each UAS if the fleet is composed of heterogeneous multirotors. The following assumption considers that the stabilization loop can only track the velocity command $v_{cmd,i}(t)$ with known precision $\bar{e}_{v,i}$, as long as the norm of the velocity command is bounded by the true speed limit $v_{\max,i}$.

Assumption 1: If $\|v_{cmd,i}(t)\| \leq v_{\max,i}$, the inner-loop velocity-tracking controller can track the velocity command $v_{cmd,i}(t)$ with known precision $\bar{e}_{v,i}$, and thus

$$\sup_{t \geq t_0} \|e_{v,i}(t)\| \leq \bar{e}_{v,i}, \qquad \forall i \in \mathcal{I}.$$

Fig. 2: Multirotor tracking the virtual target.

The following lemma uses Assumption 1, the position error dynamics, and Lyapunov theory to prove that the origin of the system in (2) is Input-to-State Stable (ISS) with respect to the velocity-tracking precision.

Lemma 1: If Assumption 1 is met, then the velocity command in Equation (4) with control gain $k_{PF,i} > 0$ ensures that the origin of the position error dynamics in Equation (2) is ISS, and the position error is bounded by

$$\|e_{p,i}(t)\| \leq \|e_{p_0,i}\| e^{-k_{PF,i}(t-t_0)} + \frac{\bar{e}_{v,i}}{k_{PF,i}} \left(1 - e^{-k_{PF,i}(t-t_0)}\right), \qquad e_{p_0,i} = e_{p,i}(t_0).$$

Remark 1: Given $\bar{e}_{v,i}$, the ultimate bound on the position error can be made arbitrarily small by increasing the value of the control gain $k_{PF,i}$. However, besides the well-known drawbacks of high-gain controllers, if the velocity command is limited by $\|v_{cmd,i}(t)\| < v_{max_i}$, then a large $k_{PF,i}$ reduces the allowable position error and mission rate that yield a feasible command

$$\|v_{cmd,i}(t)\| \leq \dot{\xi}_i(t)\, \|v_{d,i}(\xi_i(t))\| + k_{PF,i}\, \|e_{p,i}(t)\| < v_{max_i}.$$

The following section addresses the synchronization of the virtual targets to ensure the vehicles have a shared notion of the mission time, and maintain safe separation constraints during mission execution when their trajectories are temporally separated.
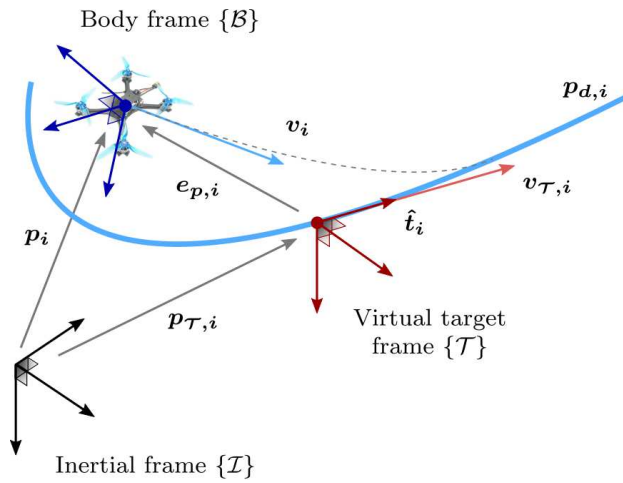
B. Time-Critical Coordination

The time-critical coordination algorithm governs the movement of the virtual targets along their paths, which is leveraged—together with the path-following error—to compute a speed command, as described in Section II-A. The objective of the time-critical coordination algorithm is to enforce coordination and temporal constraints. In this respect, previous synchronized path-following algorithms do not clearly distinguish between coordination and temporal constraints. Here, coordination refers to the agreement in the virtual times $\xi_i(t)$, and implies that agents meet desired relative position constraints such as simultaneous or sequential arrivals, specific formation patterns, or inter-agent spacing constraints as outlined in the trajectory generation phase. However, coordination constraints do not impose the time a vehicle must fly past a particular point along its path. These are temporal constraints[1]. To enforce them, a virtual entity that runs independently of all other agents is introduced, the *reference agent*. It imparts the cooperating team with the notion of a global time, and serves as a mechanism to speed up or slow down the entire mission schedule, if necessary. In pursuit of a more general architecture, only a subset of vehicles has access to the reference information—the link peers; whereas the remaining agents—the end peers—must learn that information, as depicted in Figure 3. Link and end peers are often referred to as leaders and followers in the literature. However, here we use this notation to highlight the information flow in Figure 3. Note that link peers serve as the nexus between the reference and the end peers, located at both extremes of the graph in Figure 3.
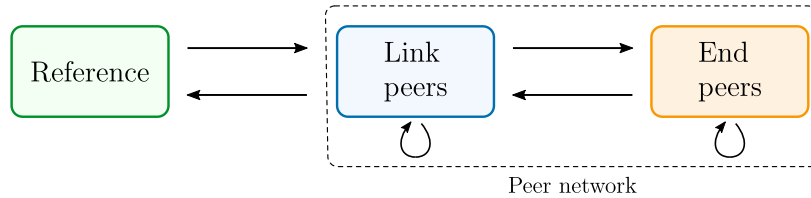

Fig. 3: Structure of the communication network and agent hierarchy.

To achieve the goal of the time-critical coordination algorithm, the UASs exchange their virtual times $\xi_i(t)$ over the network. This provides a measure of how far along the mission a vehicle is to its neighboring agents. Then, the cooperating fleet engages in a negotiation process to reach consensus on the evolution of these virtual times, which synchronizes the virtual targets. As a result, if a few UASs move ahead in the mission due to favorable winds the group in advance will slow down, whereas the group that has fallen behind will increase its pace until they catch up with their neighbors. Since the virtual times $\xi_i(t)$ define the coordination mechanism, they are also referred to as the *coordination states*. Now, to formally define the time-critical coordination problem, consider a network of n *integrator agents*

$$\dot{\xi}_i(t) = u_{c,i}(t) + u_{\mathcal{T}_\models,i}(t), \qquad i \in \mathcal{I}, \tag{5}$$

with *dynamic information flow* $\mathcal{G}(t) := (\mathcal{V}, \mathcal{E})$, where $\mathcal{V}$ represents the vertices and $\mathcal{E}(t)$ the edges of the communication graph, $\xi_i(t) \in \mathbb{R}$ is the coordination state of the ith agent, $u_{c,i}(t)$ is a coordination control input, and $u_{\mathcal{T}_\models,i}(t)$ is the long-track target-tracking error feedback[2]

$$u_{\mathcal{T}_\models,i}(t) = k_{e_p} \boldsymbol{e_{p,i}}(t) \cdot \hat{\boldsymbol{t_i}}(\xi_i(t)), \tag{6}$$

where $k_{e_p} > 0$ is a control gain, $\boldsymbol{e_{p,i}}(t) \in \mathbb{R}^3$ is the position error, and $\hat{\boldsymbol{t_i}}(t) \in \mathbb{R}^3$ is the unit tangent vector depicted in Figure 4. The target-tracking feedback is particularly relevant in cluttered

---

[1]Another way to understand these constraints is to think of coordination constraints as relative temporal constraints; and what is referred here as temporal constraints can be understood as absolute temporal constraints, like a desired arrival time or an arrival window.

[2]To aid in the interpretation of this nomenclature, all long-track errors include the subscript $\models$, as opposed to the cross-track errors that would include the subscript $\Vdash$.

scenarios. It established a negotiation process between each vehicle and its virtual target that mitigates corner rounding when the vehicle has difficulty tracking its virtual target. As shown in Figure 4, rounding corners in narrow passages can be be safety critical. Next, to enforce temporal constraints the *reference agent* is introduced with the following dynamics:

$$\dot{\xi}_R = \rho, \qquad \xi_R(0) = \xi_{R_0}, \qquad (7)$$

where $\xi_R(t) \in \mathbb{R}$ is the reference state, and ρ is a constant reference rate. This agent does not attempt coordination, but provides a global reference value so that, if desired, each $\xi_i(t)$ can be forced to converge to a neighborhood of $\xi_R(t)$. As shown in Figure 3, agents are classified by their informational needs as:

Fig. 4: Collision caused by corner rounding.

1) the *reference* who shares its state and rate with the link peers;
2) a group of n_ℓ *link peers* that have access to the reference information, but also exchange their coordination states and rates with a set of neighboring agents; and
3) the *end peers* that can only exchange their coordination states and rates with a set of neighboring agents.

Without loss of generatlity, the vehicle identification numbers are organized so that $\mathcal{I}_\ell := \{1, \ldots, n_\ell\}$ and $\mathcal{I}_e := \{n_\ell + 1, \ldots, n\}$ represent the set of link and end peers, respectively. These restrictions on the flow of information aim to capture a rather general scenario, where data from the reference may not be available to some agents. In this context, the control objective is to design a coordination control law that solves the following problem.

Definition 1 (Time-Critical Coordination Problem): Design a distributed protocol that guides the coordination, temporal, and rate errors to a neighborhood of the origin

$$\xi_i(t) - \xi_j(t) \overset{t \to \infty}{\longrightarrow} [-\Delta_c, \Delta_c], \qquad \forall i,j \in \mathcal{I}, \qquad (8a)$$

$$\xi_i(t) - \xi_R(t) \overset{t \to \infty}{\longrightarrow} [-\Delta_t, \Delta_t], \qquad \forall i \in \mathcal{I}, \qquad (8b)$$

$$\dot{\xi}_i(t) - \dot{\xi}_R \in [-\Delta_r, \Delta_r], \qquad \forall i \in \mathcal{I}, \qquad (8c)$$

where $\Delta_c(t)$, $\Delta_t(t)$, and $\Delta_r(t) \geq 0$ define the width of the coordination, temporal, and rate windows, respectively.

In the problem definition above, Equation (8a) defines the coordination constraints; Equation (8b) imposes temporal specifications, and Equation (8c) enforces bounds on the desired mission rate, which in turn defines bounds on the velocity command according to Equations (3) and (4). Two types of coordination constraints are defined, depending on the value of Δ_c:

1) *Tight coordination* denotes the system specifications when $\Delta_c \equiv 0$. This is typical of scenarios where accurately observing the desired inter-agent spacing constraints is safety-critical, such as in close proximity operations.
2) *Loose coordination* is used when $\Delta_c(t)$ is bounded and away from 0. In this case, $\Delta_c(t)$ defines an allowable coordination error, which is useful in mid and far-proximity operations.

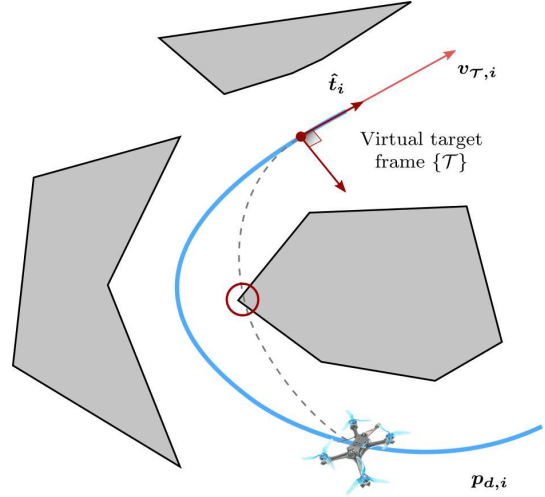Similarly, three types of temporal specifications are defined as a function of Δ_t:

1) *Unenforced temporal constraints* do not impose additional requirements, $\Delta_t \to \infty$. Thus, they are used in missions that do not require the specification of an arrival time or arrival window at any point along the path of the vehicles.

2) *Relaxed temporal specifications* encompass all $\underline{\Delta}_t \leq \Delta_t(t) \leq \overline{\Delta}_t$ bounded and away from 0, and are used to impose a desired arrival window for one or more points along the vehicle paths.

3) *Strict temporal constraints* force each $\xi_i(t)$ to track $\xi_R(t)$, $\Delta_t \equiv 0$, specifying a flyover time for each point along the vehicle path.

The spectrum of coordination and temporal specifications introduced defines six generic time-critical coordination strategies, organized according to the values of Δ_c and Δ_t. Note also that Equation (8c) indicates that the coordination rate of the ith vehicle should remain within a neighborhood of ρ. Given a mission design, the following assumption constrains the acceptable values of ρ to ensure that if everything goes as planned the norm of the speed command is smaller than the true speed limit of the vehicle.

Assumption 2: The choice of mission rate satisfies

$$\max_{t_d \in [t_{d_{init},i}, t_{d_{end},i}]} \rho \|\boldsymbol{v_{d,i}}(t_d)\| < v_{\max,i}, \qquad \forall i \in \mathcal{I}.$$

The following section addresses the assumptions on the communication network to develop a solution to the time-critical coordination problem.

C. Communication Network

For the sake of generality, we do not wish to impose any specific structure on the topology of the peer network, or assume any apriori knowledge about the amount of data exchanged among group members. Accordingly, the *peer communication network* satisfies the following general assumptions:

Assumption 3: The ith peer exchanges information with a time-varying set of peers, denoted by $\mathcal{N}_i(t) \subseteq \mathcal{I}$.

Assumption 4: Communications are bidirectional and $\xi_i(t)$ is transmitted continuously with no delays.

Assumption 5: The graph $\mathcal{G}(t)$ that models the communication network satisfies the condition

$$\frac{1}{n} \frac{1}{T} \int_t^{t+T} \bar{\boldsymbol{L}}(\tau) d\tau \geq \mu \, \mathbb{I}_{\mathbf{n-1}}, \quad \forall \, t \geq T, \tag{9}$$

where $\bar{\boldsymbol{L}}(t) := \mathbf{Q} \mathbf{L}(t) \mathbf{Q}^\top$, $\boldsymbol{L} \in \mathbb{R}^{n \times n}$ is the piecewise-constant Laplacian of $\mathcal{G}(t)$, and $\mathbf{Q} \in \mathbb{R}^{(n-1) \times n}$ satisfies $\mathbf{Q} \mathbf{1_n} = \mathbf{0}$, and $\mathbf{Q} \mathbf{Q}^\top = \mathbb{I}_{\mathbf{n-1}}$, where $\mathbf{1_n} \in \mathbb{R}^n$ is a vector of all ones.

Parameters $T > 0$ and $\mu \in (0, 1]$ characterize the Quality of Service (QoS) of the network. To aid in the interpretation of Equation (9), define and order the eigenvalues of $\mathbf{L}(t)$ such that

$$0 \equiv \lambda_1(t) \leq \lambda_2(t) \leq \ldots \leq \lambda_n(t) \leq n.$$

Then, the eigenspectrum of $\bar{\boldsymbol{L}}(t)$ is $\text{spec}\left(\bar{\boldsymbol{L}}(t)\right) = \{\lambda_2(t), \ldots, \lambda_n(t)\}$. The Fiedler eigenvalue $\lambda_2(t)$ is a measure of the algebraic connectivity, and $\lambda_2(t) > 0$ if and only if $\mathcal{G}(t)$ is connected at time t. Consequently, μ is an integral measure of the connectivity of graph $\mathcal{G}(t)$ over a sliding temporal window of width T. Equation (9) captures dynamic communication topologies arising from temporary loss of communication and switching communication links. In fact, under this condition $\mathcal{G}(t)$ may even fail to be connected pointwise in time at all times.

III. DISTRIBUTED COORDINATION CONTROL LAW

To solve the multi-objective problem for tight coordination defined in (8), the following distributed protocol is developed for the link peers:

$$u_{c,i}(t) = -k_P \sum_{j \in \mathcal{N}_i} (\xi_i(t) - \xi_j(t)) - k_R \, \omega_{R_i} (\xi_i(t) - \xi_R(t)) + \dot{\xi}_R, \qquad i \in \mathcal{I}_\ell, \tag{10}$$

TABLE I: Link-weight logic for different types of temporal constraints.

Unenforced	Relaxed		Strict
$\omega_{R_i}(t) \equiv 0$	$\omega_{R_i}(t) = \begin{cases} 1, & \text{if } |\xi_i(t) - \xi_R(t)| \geq \Delta_t(t) \ \wedge \ t - t_s^i > \tau_{R_0} \\ 0, & \text{if } |\xi_i(t) - \xi_R(t)| < \Delta_t(t) \ \wedge \ t - t_s^i > \tau_{R_1} \\ \omega_{R_i}^+(t_s^i), & \text{otherwise} \end{cases}$		$\omega_{R_i}(t) \equiv 1$

while the control law for the end peers is

$$
\begin{aligned}
u_{c,i}(t) &= -k_P \sum_{j \in \mathcal{N}_i} (\xi_i(t) - \xi_j(t)) + \chi_i(t), & i \in \mathcal{I}_e, \\
\dot{\chi}_i(t) &= -k_I \sum_{j \in \mathcal{N}_i} (\xi_i(t) - \xi_j(t)), \qquad \chi_i(0) = \chi_{i_0}, & i \in \mathcal{I}_e,
\end{aligned}
\tag{11}
$$

where k_R, k_P, and k_I are control gains, ω_{R_i} is a link weight that implements the different types of temporal constraints, and $\chi_i(t)$ is an integral state responsible for learning the mission rate $\dot{\xi}_R$. As shown in Table I, for unenforced or strict temporal constraints ω_{R_i} are identically equal to 0 or 1, respectively, thus permanently "ignoring" or "listening" to the information provided by the reference agent. However, for relaxed temporal constrains Table I defines a state-dependent switching logic that selectively "listens" to the reference agent. In this context, t_s^i denotes the last time the ith link peer switched the value of ω_{R_i}, and $\omega_{R_i}^+(t_s^i)$ is the limit from the right at t_s^i. To avoid Zeno behavior, changes in the link-weight values are subject to slow switching constraints, where dwell times τ_{R_0} and τ_{R_1} define the minimum times ω_{R_i} will be set to 0 or 1, respectively.

IV. Status of the Effort

This section utilizes the distributed protocols above, to extend previous theorems that derived conclusions for ideal target-tracking capabilities—$u_{\mathcal{T}_\models,i}(t) \equiv 0$ for all $i \in \mathcal{I}$. Assuming a fleet of heterogeneous cooperating vehicles equipped with realistic speed-tracking controllers, this section analyzes the structure of the collective target-tracking feedback. This feedback structure is then propagated through the system dynamics as a perturbation to infer transient and steady-state guarantees under non-ideal target-tracking conditions.

A. Collective Target-Tracking Feedback

To characterize the system performance with realistic and heterogeneous speed-tracking controllers, this section considers Assumption 1 and analyzes the effects of the initial position errors $\boldsymbol{e}_{p,i_0}$ and speed-tracking precision $\bar{e}_{v,i}$ on $\boldsymbol{u}_{\mathcal{T}_\models}(t)$. To this end, Lemma 1, and the fact that $\hat{\boldsymbol{t}}_i$ is a unit vector yield the following bound for target-tracking feedback:

$$
\|\boldsymbol{u}_{\mathcal{T}_\models}(t)\| \leq \bar{u}_{\mathcal{T}_\models}(t) := k_{e_p} \|\boldsymbol{e}_{p_0}\| e^{-\underline{k}_{PF} t} + \frac{k_{e_p}}{\underline{k}_{PF}} \|\bar{\boldsymbol{e}}_v\| \left(1 - e^{-\bar{k}_{PF} t}\right), \qquad \forall t \geq 0,
\tag{12}
$$

where $\boldsymbol{e}_{p_0} := [\boldsymbol{e}_{p_0,1}^\top, \boldsymbol{e}_{p_0,2}^\top, \dots, \boldsymbol{e}_{p_0,n}^\top]^\top$, $\bar{\boldsymbol{e}}_v := [\bar{e}_{v,1}, \bar{e}_{v,2}, \dots, \bar{e}_{v,n}]^\top$, $\underline{k}_{PF} := \min_{\forall i \in \mathcal{I}} k_{PF,i}$, and $\bar{k}_{PF} := \max_{\forall i \in \mathcal{I}} k_{PF,i}$. Note that the coordination control law in Equations (10) and (11) uses the same gains for all cooperating agents. However, the target-tracking feedback bound above includes individual gains $k_{PF,i}$, and speed-tracking precision bounds $\bar{e}_{v,i}$ for each agent, thus acknowledging that the

algorithms and vehicle dynamics beneath the coordination layer can be heterogeneous. Notice also, that the bound in Equation (12) has two components, depicted in Figure 5:

1) An exponentially decaying term, proportional to $\|e_{p_0}\|$, shown in orange, and induced by the speed command in (4).
2) A uniformly bounded term, proportional to $\|\bar{e}_v\|$, shown in yellow, and caused by the underlying non-ideal speed-tracking controllers.

The following section explores how the perturbation in Equation (12) propagates through the system dynamics for unenforced, relaxed, and strict temporal constraints under tight coordination.
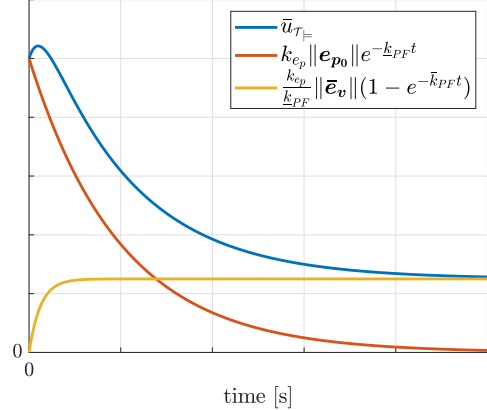
Fig. 5: Target-tracking feedback bound.

B. Stability with Non-Ideal Target Tracking

Next, previous theorems are extended to account for non-ideal speed-tracking controllers, and infer conditions that ensure the maximum speed command for each UAS is not exceeded.

1) Unenforced Temporal Constraints: building upon previous results, the link-weight logic for unenforced temporal specifications ($\omega_{R_i}(t) \equiv \mathbf{0}$) decouples the collective coordination and rate errors $\boldsymbol{\zeta_u}(t)$ from the temporal error $\zeta_t(t)$, and yields

$$\dot{\zeta}_t(t) = \boldsymbol{A_t}\boldsymbol{\zeta_u}(t) + \boldsymbol{B_t}\boldsymbol{u}_{\mathcal{T}_{\models}}(t), \qquad \zeta_t(0) = \zeta_{t_0}, \tag{13a}$$

$$\dot{\boldsymbol{\zeta}}_{\boldsymbol{u}}(t) = \boldsymbol{A_u}(t)\boldsymbol{\zeta_u}(t) + \boldsymbol{B_u}\boldsymbol{u}_{\mathcal{T}_{\models}}(t), \qquad \boldsymbol{\zeta_u}(0) = \boldsymbol{\zeta_{u_0}}, \tag{13b}$$

where $\boldsymbol{A_t}$, $\boldsymbol{A_u}(t)$, $\boldsymbol{B_t}$, and $\boldsymbol{B_u}$ are known matrices. The following theorem uses the proof of a previous theorem and perturbation theory to conclude that the temporal error in (13a) is integral Input-to-State Stable (iISS) and can grow at most linearly with time, whereas the coordination and rate errors in (13b) are λ_u-weighted iISS with respect to $\boldsymbol{u}_{\mathcal{T}_{\models}}(t)$.

Theorem 1: Assume the underlying speed-tracking controller for all agents satisfies Assumption 1, the information flow $\mathcal{G}(t)$ satisfies Assumptions 3 through 5, and the speed profiles assigned to each agent by the trajectory generation algorithms satisfy Assumption 2. If the collective speed-tracking precision satisfies

$$\|\bar{e}_v\| < \min_{i \in \mathcal{I}} \frac{v_{max,i} - \rho v_{d_{max},i}}{1 + \left(\kappa_{r,u_v} + \frac{k_{e_p}}{k_{PF}}\right) v_{d_{\max},i}},$$

then there exist known control gains k_P, k_I, and $k_{PF,i} > 0$ for all $i \in \mathcal{I}$, such that for all initial conditions $(\boldsymbol{\zeta_{u_0}}, e_{p_0}) \in \Omega_{u_0}$, the speed command in (4), with the protocol for unenforced temporal constraints in (10) and (11), ensures that

$$\|\boldsymbol{v_{cmd,i}}(t)\| \leq v_{max,i}, \qquad \forall t \geq 0, \qquad \forall i \in \mathcal{I},$$

and the individual temporal, coordination, and rate errors satisfy

$$\begin{bmatrix} |\xi_i(t) - \xi_R(t)| \\ |\xi_i(t) - \xi_j(t)| \\ |\dot{\xi}_i(t) - \rho| \end{bmatrix} \leq \boldsymbol{K_u}(t) \begin{bmatrix} |\zeta_{t_0}| \\ \|\boldsymbol{\zeta_{u_0}}\| \\ \|e_{p_0}\| \\ \|\bar{e}_v\| \end{bmatrix}, \qquad \forall t \geq 0, \qquad \forall i, j \in \mathcal{I},$$

where $\boldsymbol{K_u}(t) \in \mathbb{R}^{3\times 4}$ is defined as

$$\boldsymbol{K_u} := \begin{bmatrix} 1 & \kappa_{t,u_1}e^{-\lambda_u t} + \kappa_{t,u_2} & \frac{\kappa_{t,u_{p_1}}}{\lambda_u - \underline{k}_{PF}}\left(e^{-\underline{k}_{PF}t} - e^{-\lambda_u t}\right) + \kappa_{t,u_{p_2}} & \kappa_{t,u_{v_1}} + \kappa_{t,u_{v_2}}t \\[1em] 0 & \kappa_{c,u}e^{-\lambda_u t} & \frac{\kappa_{c,u_p}}{\lambda_u - \underline{k}_{PF}}\left(e^{-\underline{k}_{PF}t} - e^{-\lambda_u t}\right) & \kappa_{c,u_v} \\[1em] 0 & \kappa_{r,u}e^{-\lambda_u t} & \frac{\kappa_{r,u_p}}{\lambda_u - \underline{k}_{PF}}\left(e^{-\underline{k}_{PF}t} - e^{-\lambda_u t}\right) + k_{e_p}e^{-\underline{k}_{PF}t} & \kappa_{r,u_v} + \frac{k_{e_p}}{\underline{k}_{PF}} \end{bmatrix},$$

Ω_{u_0} is a known non-empty set, κ_{t,u_1}, κ_{t,u_2}, $\kappa_{t,u_{p_1}}$, $\kappa_{t,u_{p_2}}$, $\kappa_{t,u_{v_1}}$, $\kappa_{t,u_{v_2}}$, $\kappa_{c,u}$, κ_{c,u_p}, κ_{c,u_v}, $\kappa_{r,u}$, κ_{r,u_p}, and κ_{r,u_v} are known constants, and $\lambda_u = \nu\underline{\lambda}_u$ is the guaranteed rate of convergence with $\nu = 1$.

To help in the interpretation of Theorem 1, the elements in matrix $\boldsymbol{K_u}(t)$ have been color coded and organized into groups with similar behavior and origin:

1) The elements in   blue   are exponentially decaying.

2) The block in   purple   represents the interaction between the dynamics of $\boldsymbol{\zeta_u}(t)$ in Equation (13) with the position error dynamics in Equation (2). Note that these terms are always positive semidefinite for all $t \geq 0$.

3) The terms in   orange   define ultimate bounds that are proportional to $\|\bar{\boldsymbol{e}}_{\boldsymbol{v}}\|$, whereas the terms in   yellow   denote ultimate bounds that are proportional to $\|\boldsymbol{\zeta}_{\boldsymbol{u_0}}\|$ and $\|\boldsymbol{e}_{\boldsymbol{p_0}}\|$. Two important conclusions follow:

- Tight coordination cannot be attained unless the speed tracking error of each agent converges to the origin, $\|\boldsymbol{e}_{\boldsymbol{v,i}}(t)\| \to 0$ as $t \to \infty$ for all $i \in \mathcal{I}$.
- The coordinating agents cannot accurately learn the mission rate unless the speed tracking error of each agent converges to the origin, $\|\boldsymbol{e}_{\boldsymbol{v,i}}(t)\| \to 0$ as $t \to \infty$ for all $i \in \mathcal{I}$.

This emphasizes the importance of the control laws underneath the coordination layer. The implementation of a control law that tracks the speed command in Equation (4) with accuracy will tighten the ultimate bounds for $|\xi_i(t) - \xi_j(t)|$ and $|\dot{\xi}_i(t) - \rho|$.

4) The element in   red   indicates that the temporal error can drift away over time, and this drift is proportional to $\|\bar{\boldsymbol{e}}_{\boldsymbol{v}}\|$.

5) The terms in   green   are a direct effect of $\boldsymbol{u}_{\mathcal{T}_{\models}}(t)$, and can be easily identified with the elements in Equatiom (12).

The following section derives transient and steady-state performance guarantees for relaxed temporal constraints with non-ideal target tracking capabilities.

2) Relaxed Temporal Constraints: again building upon previous results, the dynamics for relaxed temporal constraints can be rewritten as a system that switches between modes $\varnothing$ and $\bigcirc$, with switching signal $\gamma(t) : [0, \infty) \mapsto \mathcal{S}$, and $\mathcal{S} := \{\varnothing, \bigcirc\}$

$$\dot{\boldsymbol{\zeta}}(t) = \boldsymbol{A}_\gamma(t)\boldsymbol{\zeta}(t) + \boldsymbol{B}\boldsymbol{u}_{\mathcal{T}_{\models}}(t), \qquad \boldsymbol{\zeta}(0) = \boldsymbol{\zeta_0}, \qquad \gamma \in \mathcal{S}, \tag{14}$$

where $\boldsymbol{A}_\varnothing$, $\boldsymbol{A}_{\bigcirc}$, and $\boldsymbol{B}$ are known. The system is in empty mode $\varnothing$ when the set of link peers that decide to listen to the reference agent is empty. The cloud mode $\bigcirc$ encompasses all cases where at least one link peer listens to the reference agent. The discontinuities in $\gamma(t)$ occur at the switching times t_m, with $m \in \mathbb{N}$. Recall Theorem 1 proves $|\xi_i(t) - \xi_R(t)|$ can drift away in mode $\varnothing$. Then, anticipating that τ_{R_1} may be a function of the time spent in mode $\varnothing$, a subtle change in the link-weight logic is

introduced

$$\omega_{R_i}(t) = \begin{cases} 1, & \text{if } |\xi_i(t) - \xi_R(t)| \geq \Delta_t(t) \ \wedge \ t - t_s^i > \tau_{R_0}, \\ 0, & \text{if } |\xi_i(t) - \xi_R(t)| < \Delta_t(t) \ \wedge \ t - t_s^i > \tau_{R_1}^i(\Delta t_0^i(t)), \\ \omega_{R_i}^+(t_s^i), & \text{otherwise,} \end{cases} \qquad (15)$$

where $\Delta t_0^i(t)$ is defined as follows:

$$\Delta t_0^i(t) := \begin{cases} t_s^i - t_{s-1}^i, & \text{if } \omega_{R_i}(t) = 1, \\ 0, & \text{if } \omega_{R_i}(t) = 0. \end{cases}$$

As depicted in Figure 6, t_s^i and t_{s-1}^i respectively denote the last and second to last times the ith link peer switched the value of $\omega_{R_i}(t)$. Part of the challenge is that link peers ignore the time spent in mode $\varnothing$, and hence can only use $\Delta t_0^i(t)$ to counteract the drift of the collective system. Then, assuming $\gamma(t_0) = \varnothing$ and expressing m in terms of the number of $\varnothing$-☁ cycles completed k, the logic above can only enforce the following slow switching constraints for the system dynamics:

$$\left. \begin{array}{rcl} t_{2k} - t_{2k-1} & > & \tau_{R_{1,k}}, \\ t_{2k-1} - t_{2k-2} & \geq & 0, \end{array} \right\} \qquad (16)$$

where $\tau_{R_{1,k}} := \max_{i \in \mathcal{I}_\ell} \tau_{R_1}^i(t_{2k-1})$. Note that each agent implements a different dwell time $\tau_{R_1}^i(t)$, and the collective dwell time $\tau_{R_{1,k}}$ varies with each $\varnothing$-☁ cycle.

The following lemma uses previous results and perturbation theory to analyze the system in mode ☁, and concludes that the dynamics in (14) are λ_r-weighted iISS with respect to $\boldsymbol{u}_{\mathcal{T}_\models}(t)$.

Fig. 6: Consecutive weight switches.

Lemma 2: Assume the underlying speed-tracking controller for all agents satisfies Assumption 1, the information flow $\mathcal{G}(t)$ satisfies Assumptions 3 through 5, and $\tilde{\omega}(t) \geq 1$. Then, there exist known control gains k_R, k_P, k_I, and $k_{PF,i} > 0$ for all $i \in \mathcal{I}$ such that

$$\begin{bmatrix} |\xi_i(t) - \xi_R(t)| \\ |\xi_i(t) - \xi_j(t)| \\ |\dot{\xi}_i(t) - \rho| \end{bmatrix} \leq \boldsymbol{K_r}(t) \begin{bmatrix} \|\boldsymbol{\zeta_0}\| \\ \|\boldsymbol{e_{p_0}}\| \\ \|\bar{\boldsymbol{e}}_{\boldsymbol{v}}\| \end{bmatrix}, \qquad \forall t \geq 0, \qquad \forall i, j \in \mathcal{I},$$

where $\boldsymbol{K_r}(t) \in \mathbb{R}^{3 \times 3}$ is defined as

$$\boldsymbol{K_r}(t) := \begin{bmatrix} \kappa_{t,r} e^{-\lambda_r t} & \frac{\kappa_{t,r_p}}{\lambda_r - \underline{k}_{PF}} \left(e^{-\underline{k}_{PF} t} - e^{-\lambda_r t} \right) & \kappa_{t,r_v} \\ \kappa_{c,r} e^{-\lambda_r t} & \frac{\kappa_{c,r_p}}{\lambda_r - \underline{k}_{PF}} \left(e^{-\underline{k}_{PF} t} - e^{-\lambda_r t} \right) & \kappa_{c,r_v} \\ \kappa_{r,r} e^{-\lambda_r t} & \frac{\kappa_{r,r_p}}{\lambda_r - \underline{k}_{PF}} \left(e^{-\underline{k}_{PF} t} - e^{-\lambda_r t} \right) + k_{e_p} e^{-\underline{k}_{PF} t} & \kappa_{r,r_v} + \frac{k_{e_p}}{\underline{k}_{PF}} \end{bmatrix},$$

$\kappa_{t,r}$, κ_{t,r_p}, κ_{t,r_v}, $\kappa_{c,r}$, κ_{c,r_p}, κ_{c,r_v}, $\kappa_{r,r}$, κ_{r,r_p}, κ_{r,r_v} are known constants, and λ_r is the guaranteed rate of convergence.

The elements in matrix $\boldsymbol{K_r}(t)$ have been color coded using the same criteria as in Section IV-B1. The most notable differences between $\boldsymbol{K_u}(t)$ and $\boldsymbol{K_r}(t)$ are that in matrix $\boldsymbol{K_r}(t)$ the ultimate bounds
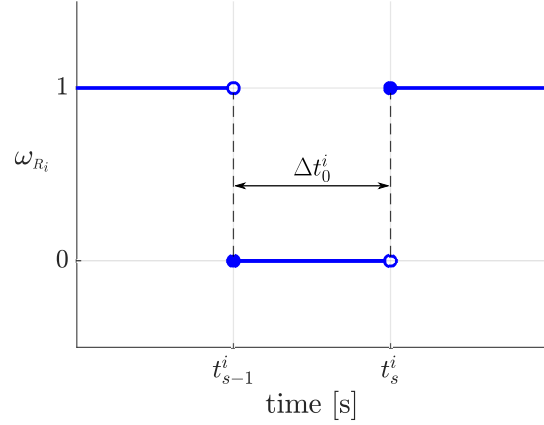
in <mark>yellow,</mark> and the drifting term in <mark>red</mark> have vanished. As a result, the steady-state value of the temporal error $|\xi_i(t) - \xi_R(t)|$ in mode ☁ is proportional to $\|\bar{e}_v\|$. The next corollary follows from this analysis.

Corollary 1: Given the assumptions in Lemma 2, if the collective speed-tracking error satisfies

$$\|\bar{e}_v\| \leq \frac{\Delta_t}{\kappa_{t,r_v}},$$

then there exists a time $t_{\Delta_t} \geq 0$ such that

$$|\xi_i(t) - \xi_R(t)| \leq \Delta_t(t), \qquad \forall t \geq t_{\Delta_t}, \qquad \forall i \in \mathcal{I}.$$

So far, modes $\varnothing$ and ☁ have been analyzed separately in Theorem 1 and Lemma 2, respectively. The following theorem combines these results, perturbation and switched systems theory, and convergence properties of infinite series to find $\tau_{R_1}^i(t)$. The theorem indicates that the switched system dynamics in (14) are Lyapunov stable and can persistently switch between modes $\varnothing$ and ☁.

Theorem 2: Assume the underlying speed-tracking controller for all agents satisfies Assumption 1, the information flow $\mathcal{G}(t)$ satisfies Assumptions 3 through 5, and the speed profiles assigned to each agent by the trajectory generation algorithms satisfy Assumption 2. If the desired temporal window satisfies

$$\bar{\Delta}_t < \min_{i \in \mathcal{I}} \frac{1}{\kappa_{r,r}} \left(\frac{v_{\max,i}}{v_{d_{\max},i}} - \rho \right),$$

and the collective speed-tracking error satisfies

$$\|e_v\| < \min_{i \in \mathcal{I}} \left\{ \frac{v_{\max,i} - \rho v_{d_{\max},i}}{\tilde{\kappa}_{\Omega_{u_v,i}}}, \frac{v_{\max,i} - \left(\rho + \kappa_{r,r}\bar{\Delta}_t\right) v_{d_{\max},i}}{\tilde{\kappa}_{\Omega_{r_v,i}}} \right\},$$

then there exist known control gains k_R, k_P, k_I, and $k_{PF,i} > 0$ for all $i \in \mathcal{I}$, and individual dwell times

$$\tau_{R_1}^i(t) = \max \left\{ \epsilon_\tau, \frac{1}{\lambda_r} \ln \Delta t_0^i(t) \right\} + \max \left\{ 0, \frac{1}{\lambda_r} \ln \kappa_{W_r} \right\}, \qquad \forall \in \mathcal{I}_\ell,$$

such that for all initial conditions $(\zeta_0, e_{p_0}) \in \tilde{\Omega}_0$, the speed command in (4), with the protocol in (10) and (11), and the switching logic in (15) ensure that

$$\|v_{cmd,i}(t)\| \leq v_{max,i}, \qquad \forall t \geq 0, \qquad \forall i \in \mathcal{I},$$

and $\gamma(t)$ can switch between $\varnothing$ and ☁ finitely many times in every bounded time interval. The temporal, coordination, and rate errors at the switching times from mode ☁ to $\varnothing$ satisfy

$$\begin{bmatrix} |\xi_i(t_{2k}) - \xi_R(t_{2k})| \\ |\xi_i(t_{2k}) - \xi_j(t_{2k})| \\ |\dot{\xi}_i(t_{2k}) - \rho| \end{bmatrix} \leq \tilde{K}(k) \begin{bmatrix} \|\zeta_0\| \\ \|e_{p_0}\| \\ \|\bar{e}_v\| \end{bmatrix}, \qquad \forall i, j \in \mathcal{I}, \qquad k \in \mathbb{N}.$$

In mode $\varnothing$, the temporal, coordination, and rate errors satisfy

$$\begin{bmatrix} |\xi_i(t) - \xi_R(t)| \\ |\xi_i(t) - \xi_j(t)| \\ |\dot{\xi}_i(t) - \rho| \end{bmatrix} \leq K_u(t - t_{2k-2}) \begin{bmatrix} |\zeta_t(t_{2k-2})| \\ \|\zeta_u(t_{2k-2})\| \\ \|e_p(t_{2k-2})\| \\ \|\bar{e}_v\| \end{bmatrix}, \quad \forall t_{2k-2} \leq t < t_{2k-1}, \quad \forall i, j \in \mathcal{I}, \quad k \in \mathbb{N},$$

whereas in mode ☁ the temporal, coordination, and rate errors satisfy

$$\begin{bmatrix} |\xi_i(t) - \xi_R(t)| \\ |\xi_i(t) - \xi_j(t)| \\ |\dot{\xi}_i(t) - \rho| \end{bmatrix} \leq K_r(t - t_{2k-1}) \begin{bmatrix} \|\zeta(t_{2k-1})\| \\ \|e_p(t_{2k-1})\| \\ \|\bar{e}_v\| \end{bmatrix}, \quad \forall t_{2k-1} \leq t \leq t_{2k}, \quad \forall i, j \in \mathcal{I}, \quad k \in \mathbb{N},$$

where $\boldsymbol{K_u}(t)$ and $\boldsymbol{K_r}(t)$ are defined in Theorem 1 and Lemma 2, respectively, and $\tilde{\boldsymbol{K}}(k) \in \mathbb{R}^{3 \times 3}$ is

$$\tilde{\boldsymbol{K}}(k) := \begin{bmatrix} \kappa_{t,r} e^{-k\lambda_r \epsilon_\tau} & \tilde{\kappa}_{t,p}\, k\, e^{-k\tilde{\lambda}\epsilon_\tau} & \left(\tilde{\kappa}_{t,v_1} + \tilde{\kappa}_{t,v_2} e^{\lambda_r \epsilon_\tau} \right) \sum_{m=1}^{k} e^{-m\lambda_r \epsilon_\tau} \\ \kappa_{c,r} e^{-k\lambda_r \epsilon_\tau} & \tilde{\kappa}_{c,p}\, k\, e^{-k\tilde{\lambda}\epsilon_\tau} & \left(\tilde{\kappa}_{c,v_1} + \tilde{\kappa}_{c,v_2} e^{\lambda_r \epsilon_\tau} \right) \sum_{m=1}^{k} e^{-m\lambda_r \epsilon_\tau} \\ \kappa_{r,r} e^{-k\lambda_r \epsilon_\tau} & \tilde{\kappa}_{r,p}\, k\, e^{-k\tilde{\lambda}\epsilon_\tau} + k_{e_p} e^{-k\,\underline{k}_{PF}\,\epsilon_\tau} & \left(\tilde{\kappa}_{r,v_1} + \tilde{\kappa}_{r,v_2} e^{\lambda_r \epsilon_\tau} \right) \sum_{m=1}^{k} e^{-m\lambda_r \epsilon_\tau} + \frac{k_{e_p}}{\underline{k}_{PF}} \end{bmatrix},$$

$\epsilon_\tau > 0$ is a design parameter, $\tilde{\Omega}_0$ is a known non-empty set, $\tilde{\kappa}_{\Omega_{u_v},i}$, $\tilde{\kappa}_{\Omega_{r_v},i}$, κ_{W_r}, $\kappa_{t,r}$, $\tilde{\kappa}_{t,p}$, $\tilde{\kappa}_{t,v_1}$, $\tilde{\kappa}_{t,v_2}$, $\kappa_{c,r}$, $\tilde{\kappa}_{c,p}$, $\tilde{\kappa}_{c,v_1}$, $\tilde{\kappa}_{c,v_2}$, $\kappa_{r,r}$, $\tilde{\kappa}_{r,p}$, $\tilde{\kappa}_{r,v_1}$, and $\tilde{\kappa}_{r,v_2}$, $\tilde{\lambda} := \min\{\underline{k}_{PF}, \lambda_r\}$, and λ_r is the guaranteed rate of convergence in mode ☁.

The elements in matrix $\tilde{\boldsymbol{K}}(k)$ have been color coded using the same criteria as in Section IV-B1. Note that the propagation of the perturbation in (12) through the switched system presents structural similarities with the results in mode ☁. This becomes clear if one compares matrices $\boldsymbol{K_r}(t)$ and $\tilde{\boldsymbol{K}}(k)$. They contain the same-color blocks in the same locations. As shown in Figure 7, the elements in $\tilde{\boldsymbol{K}}(k)$ behave as follows:

1) The blocks in blue decrease exponentially with k, the number of ∅-☁ cycles.

2) The elements in purple are dominated by a linear growth for small k, and an exponential decay for large k.

3) The terms in orange are ultimately bounded. Application of D'Alembert's criterion proves convergence of this infinite series.

4) The terms in green are a direct effect of $\boldsymbol{u}_{\mathcal{T}_\models}(t)$ as it propagates through the switched system, and can be easily identified with the elements in Equatiom (12).

In all cases, we observe a similar behavior as their continuous counter parts in $\boldsymbol{K_r}(t)$.

The following corollary follows from Lemma 2 and Theorem 2, and concludes that if the collective speed-tracking error satisfies certain conditions, then two possible behaviors may emerge from the switching logic in Equation (15) either

1) After some time t_{Δ_t} the switched system (14) stays in mode ∅, $|\xi_i(t) - \xi_R(t)|$ remains within $\Delta_t(t)$ for all link peers, and $|\xi_i(t) - \xi_R(t)|$ is bounded for all end peers but may lie outside $\Delta_t(t)$; or

2) The switched system (14) persistently switches between modes ∅ and ☁. In this case, there exists a number of ∅-☁ cycles k_{Δ_t} beyond which the temporal error $|\xi_i(t_{2k}) - \xi_R(t_{2k})|$ falls inside $\Delta_t(t_{2k})$ for all agents. Between switching times t_{2k} and t_{2k+2}, $|\xi_i(t) - \xi_R(t)|$ remains bounded, but some agents will depart the desired temporal window $\Delta_t(t)$.
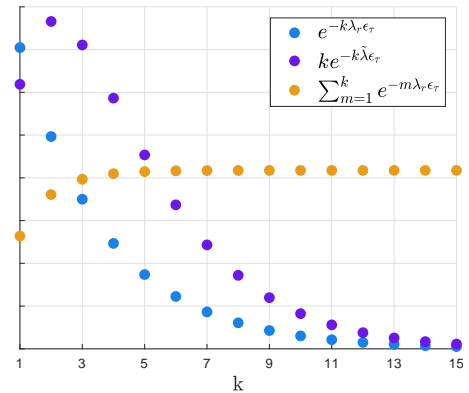

Fig. 7: Response of the terms in $\tilde{\boldsymbol{K}}$.

Corollary 2: Given the assumptions in Theorem 2, if the collective speed-tracking error satisfies

$$\|\bar{\boldsymbol{e}}_{\boldsymbol{v}}\| \leq \Delta_t \min \left\{ \frac{1}{\kappa_{t,r_v}}, \frac{e^{\lambda_r \epsilon_\tau} - 1}{\tilde{\kappa}_{t,v_1} + \tilde{\kappa}_{t,v_2} e^{\lambda_r \epsilon_\tau}} \right\},$$

then two behaviors may emerge for the switched system (14) either

13

1) There exists a time t_{Δ_t} such that $\gamma(t) = \varnothing$ for all $t \geq t_{\Delta_t}$, and

$$|\xi_i(t) - \xi_R(t)| < \Delta_t(t), \qquad \forall t \geq t_{\Delta_t}, \qquad \forall i \in \mathcal{I}_\ell,$$

$$|\xi_i(t) - \xi_R(t)| < \Delta_t(t) + \kappa_{c,u}\|\boldsymbol{\zeta_u}(t_{\Delta_t})\|e^{-\lambda_u(t-t_{\Delta_t})} + \ldots$$

$$+ \frac{\kappa_{c,u_p}}{\underline{k}_{PF} - \lambda_u}\|\boldsymbol{e_p}(t_{\Delta_t})\| \left(e^{-\lambda_u(t-t_{\Delta_t})} - e^{-\underline{k}_{PF}(t-t_{\Delta_t})}\right) + \ldots$$

$$+ \kappa_{c,u_v}\|\bar{\boldsymbol{e}}_{\boldsymbol{v}}\|, \qquad \forall t \geq t_{\Delta_t}, \qquad \forall i \in \mathcal{I}_e; \qquad \text{or}$$

2) $\gamma(t)$ persistently switches between modes $\varnothing$ and ☁, and there exists a $k_{\Delta_t} \in \mathbb{N}$ such that

$$|\xi_i(t_{2k}) - \xi_R(t_{2k})| \leq \Delta_t(t_{2k}), \qquad \forall k \geq k_{\Delta_t}, \qquad \forall i \in \mathcal{I},$$

and the temporal errors $|\xi_i(t) - \xi_R(t)|$ between t_{2k} and t_{2k+2} in modes $\varnothing$ and ☁ are bounded for all agents.

According to Theorem 1 the temporal error can drift away from the origin in mode $\varnothing$. However, Theorem 1 only provides an upper bound for the evolution of $|\xi_i(t) - \xi_R(t)|$, and therefore does not guarantee that the temporal errors will indeed drift. This is relevant in the interpretation of Corollary 2 because if $|\xi_i(t) - \xi_R(t)|$ indeed drifts, then the only compatible behavior is item ii). The real implementation of this cooperative system will drift in mode $\varnothing$, because the vehicle speed-tracking controllers will invariably incur in small tracking errors. Hence, the real system will exhibit persistent switches between modes $\varnothing$ and ☁. Therefore, item i) in the corollary is a result of the formality of this proof. One may attempt to remove it assuming the following PE-like conditions involving the speed-tracking error:

$$\frac{1}{T_v} \int_t^{t+T_v} \boldsymbol{e}_{\boldsymbol{v,i}}^\top(\tau)\boldsymbol{e}_{\boldsymbol{v,i}}(\tau)\mathrm{d}\tau \geq \mu_v, \qquad \forall t \geq T_v, \qquad i \in \mathcal{I},$$

with $T_v > 0$ and $\mu_v > 0$, and the QoS of the communication network:

$$\frac{1}{n}\frac{1}{T} \int_t^{t+T} \bar{\boldsymbol{L}}(\tau)d\tau \leq \bar{\mu}\,\mathbb{I}_{\boldsymbol{n-1}}, \quad \forall\, t \geq T,$$

with $T > 0$ and $\mu \leq \bar{\mu} \in (0, 1]$. In accordance with the expected behavior, the following remark analyzes the performance guarantees as the number of $\varnothing$-☁ cycles increases.

Remark 2: As the number of $\varnothing$-☁ cycles increases, the switched system (14) successfully cancels out the effects of the initial error $\|\boldsymbol{\zeta_0}\|$ and position-tracking errors $\|\boldsymbol{e_{p_0}}\|$ as shown next

$$\lim_{k \to \infty} \begin{bmatrix} |\xi_i(t_{2k}) - \xi_R(t_{2k})| \\ |\xi_i(t_{2k}) - \xi_j(t_{2k})| \\ |\dot{\xi}_i(t_{2k}) - \rho| \end{bmatrix} \leq \begin{bmatrix} \tilde{\kappa}_{t,v_1} + \tilde{\kappa}_{t,v_2}e^{\lambda_r \epsilon_\tau} \\ \tilde{\kappa}_{c,v_1} + \tilde{\kappa}_{c,v_2}e^{\lambda_r \epsilon_\tau} \\ \tilde{\kappa}_{r,v_1} + \tilde{\kappa}_{r,v_2}e^{\lambda_r \epsilon_\tau} \end{bmatrix} \frac{1}{e^{\lambda_r \epsilon_\tau} - 1}\|\bar{\boldsymbol{e}}_{\boldsymbol{v}}\|.$$

Thus, increasing the value of ϵ_τ cannot completely eliminate the error induced by $\|\bar{\boldsymbol{e}}_{\boldsymbol{v}}\|$, but can reduce it to some extent, since $\frac{1}{e^{\lambda_r \epsilon_\tau} - 1}$ and $\frac{e^{\lambda_r \epsilon_\tau}}{e^{\lambda_r \epsilon_\tau} - 1}$ are monotonically decreasing, and

$$\lim_{\epsilon_\tau \to \infty} \frac{1}{e^{\lambda_r \epsilon_\tau} - 1} = 0, \qquad \text{and} \qquad \lim_{\epsilon_\tau \to \infty} \frac{e^{\lambda_r \epsilon_\tau}}{e^{\lambda_r \epsilon_\tau} - 1} = 1.$$

When the value of ϵ_τ is increased the contributions of mode $\varnothing$ to the temporal, coordination, and rate errors diminish, since the system stays in mode ☁ for longer periods of time.

The following section derives transient and steady-state performance guarantees for strict temporal constraints with non-ideal target tracking capabilities.

DISTRIBUTION A: Distribution approved for public release.

3) Strict Temporal Constraints: the link-weight logic in Table I for strict temporal specifications $(\omega_{R_i}(t) \equiv 1)$ can be leveraged to simplify the system dynamics, and yields the following theorem, which uses previous results and perturbation theory to prove that the origin of the system dynamics is λ_s-weighted iISS with respect to $\boldsymbol{u}_{\mathcal{T}_\models}(t)$.

Theorem 3: Assume the underlying speed tracking-controller for all agents satisfies Assumption 1, the information flow $\mathcal{G}(t)$ satisfies Assumptions 3 through 5, and the speed profiles assigned to each agent by the trajectory generation algorithms satisfy Assumption 2. If the collective speed-tracking precision satisfies

$$\|\bar{\boldsymbol{e}}_{\boldsymbol{v}}\| < \min_{i \in \mathcal{I}} \frac{v_{max,i} - \rho v_{d_{max},i}}{1 + \left(\kappa_{r,s_v} + \frac{k_{e_p}}{\underline{k}_{PF}}\right) v_{d_{\max},i}},$$

then there exist known control gains k_R, k_P, k_I, and $k_{PF,i} > 0$ for all $i \in \mathcal{I}$, such that for all initial conditions $(\boldsymbol{\zeta_0}, \boldsymbol{e_{p_0}}) \in \Omega_{s_0}$, the speed command in (4), with the protocol for strict temporal constraints in (10) and (11) ensure that

$$\|\boldsymbol{v_{cmd,i}}(t)\| \leq v_{max,i}, \qquad \forall t \geq 0, \qquad \forall i \in \mathcal{I},$$
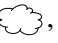
and the individual temporal, coordination, and rate errors satisfy

$$\begin{bmatrix} |\xi_i(t) - \xi_R(t)| \\ |\xi_i(t) - \xi_j(t)| \\ |\dot{\xi}_i(t) - \rho| \end{bmatrix} \leq \boldsymbol{K_s}(t) \begin{bmatrix} \|\boldsymbol{\zeta_0}\| \\ \|\boldsymbol{e_{p_0}}\| \\ \|\bar{\boldsymbol{e}}_{\boldsymbol{v}}\| \end{bmatrix}$$

where $\boldsymbol{K_s}(t) \in \mathbb{R}^{3 \times 3}$ is defined as

$$\boldsymbol{K_s}(t) := \begin{bmatrix} \kappa_{t,s} e^{-\lambda_s t} & \frac{\kappa_{t,s_p}}{\lambda_s - \underline{k}_{PF}}\left(e^{-\underline{k}_{PF}t} - e^{-\lambda_s t}\right) & \kappa_{t,s_v} \\ \kappa_{c,s} e^{-\lambda_s t} & \frac{\kappa_{c,s_p}}{\lambda_s - \underline{k}_{PF}}\left(e^{-\underline{k}_{PF}t} - e^{-\lambda_s t}\right) & \kappa_{c,s_v} \\ \kappa_{r,s} e^{-\lambda_s t} & \frac{\kappa_{r,s_p}}{\lambda_s - \underline{k}_{PF}}\left(e^{-\underline{k}_{PF}t} - e^{-\lambda_s t}\right) + k_{e_p} e^{-\underline{k}_{PF}t} & \kappa_{r,s_v} + \frac{k_{e_p}}{\underline{k}_{PF}} \end{bmatrix}.$$

Ω_{s_0} is a known non-empty set, $\kappa_{t,s}$, κ_{t,s_p}, κ_{t,s_v}, $\kappa_{c,s}$, κ_{c,s_p}, κ_{c,s_v}, $\kappa_{r,s}$, κ_{r,s_p}, and κ_{r,s_v} are known constants, and λ_s is the guaranteed rate of convergence.

The elements in matrix $\boldsymbol{K_s}(t)$ have been color coded using the same criteria as in Section IV-B1. Notice also that $\boldsymbol{K_s}(t)$ has the same structure as $\boldsymbol{K_r}(t)$, but with different constants and rate of convergence. The reason for this resemblance is that strict temporal constraints are a particular case of mode ☁, where all link peers listen to the reference agent at all times.

C. Safety Criticality of the Coordination Protocols

Consider now a pair of UAS with identification numbers i and j, equipped with the coordinated path-following algorithms described so far. The time-critical coordination algorithm has two feedback terms, both of importance for the safety of the cooperating peers: the coordination feedback $\boldsymbol{u_c}(t)$ attempts to synchronize the virtual targets to ensure safe separation among the UAS; and the target-tracking feedback $\boldsymbol{u}_{\mathcal{T}_\models}(t)$ slows or expedites the progress of the virtual targets along their trajectories if the actual vehicles are behind or ahead their targets. This establishes a negotiation process between the agents and their virtual targets that prevents vehicles from "cutting corners", and thus avoids potential collisions with nearby obstacles, particularly in cluttered environments. These vehicles are also assigned time-deconflicted trajectories, as illustrated in Figure 8, that is

$$\|\boldsymbol{p_{d,i}}(t_d) - \boldsymbol{p_{d,j}}(t_d)\| \geq d_s, \qquad \forall t_d \in [t_{d_{init}}, t_{d_{end}}], \qquad i, j \in \mathcal{I}, \qquad i \neq j.$$
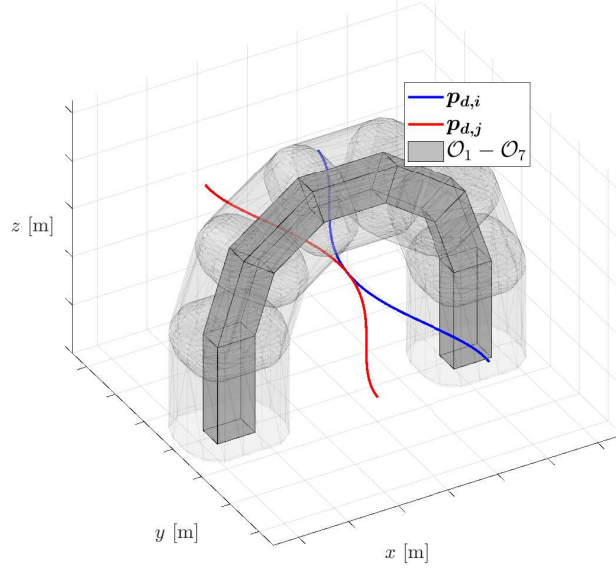
Fig. 8: Time-deconflicted trajectories.

Generally, the initial and final times of a pair of trajectories may not coincide. As a result, trajectories represented as a sequence of Bézier curves can be clipped accordingly using de Casteljau's algorithm so that the initial and final times of the trajectory segments being compared coincide, as in the equation above. The safety distance used to deconflict these trajectories in the trajectory generation phase

$$d_s = c_s \left(d_{p,i} + d_{p,j} \right),$$

is informed with the uncertainty distances $d_{p,i}$ and $d_{p,j}$, which account for the dimensions of the vehicle frames, and expected target-tracking errors under nominal conditions. The safety factor $c_s > 1$ provides an additional safety buffer for unmodeled errors. The desired trajectories and the coordination states of the UASs at time t determine the position of the virtual targets

$$\boldsymbol{p_{\tau,i}}(t) := \boldsymbol{p_{d,i}}(\xi_i(t)), \qquad \boldsymbol{p_{\tau,j}}(t) := \boldsymbol{p_{d,j}}, (\xi_j(t)).$$

In addition, Lemma 1 provides a bound for the target-tracking errors as a function of time, which can be further simplified as follows:

$$\|\boldsymbol{e_{p,i}}(t)\| \leq \|\boldsymbol{e_{p,i_0}}\| e^{-k_{PF,i}(t-t_{d_{init}})} + \frac{\bar{e}_{v,i}}{k_{PF,i}}, \qquad \|\boldsymbol{e_{p,j}}(t)\| \leq \|\boldsymbol{e_{p,j_0}}\| e^{-k_{PF,j}(t-t_{d_{init}})} + \frac{\bar{e}_{v,j}}{k_{PF,j}}. \quad (17)$$

These expressions define two balls centered at each of the virtual targets with a monotonically decreasing radius over time, which serve as bounding regions for the center of mass of each agent. As the virtual targets move, these balls define a pair of shrinking tubes, as illustrated in Figure 9. Consequently, the distance between the centers of mass of vehicles i and j can be bounded by

$$\begin{aligned} \|\boldsymbol{p_i}(t) - \boldsymbol{p_j}(t)\| &= \|\boldsymbol{p_{\tau,i}}(t) + \boldsymbol{e_{p,i}}(t) - \boldsymbol{p_{\tau,j}}(t) - \boldsymbol{e_{p,j}}(t)\| \\ &\geq \|\boldsymbol{p_{d,i}}(\xi_i(t)) - \boldsymbol{p_{d,j}}(\xi_j(t))\| - \|\boldsymbol{e_{p,i}}(t)\| - \|\boldsymbol{e_{p,j}}(t)\|. \end{aligned} \quad (18)$$

If the virtual targets were perfectly coordinated, that is $\xi_i(t) \equiv \xi_j(t)$, then the distance between the virtual targets would be $\|\boldsymbol{p_{d,i}}(\xi_i(t)) - \boldsymbol{p_{d,j}}(\xi_j(t))\| \geq d_s$ for all $\xi_i, \xi_j \in [t_{d_{init}}, t_{d_{end}}]$. However, Theorems 1, 2,
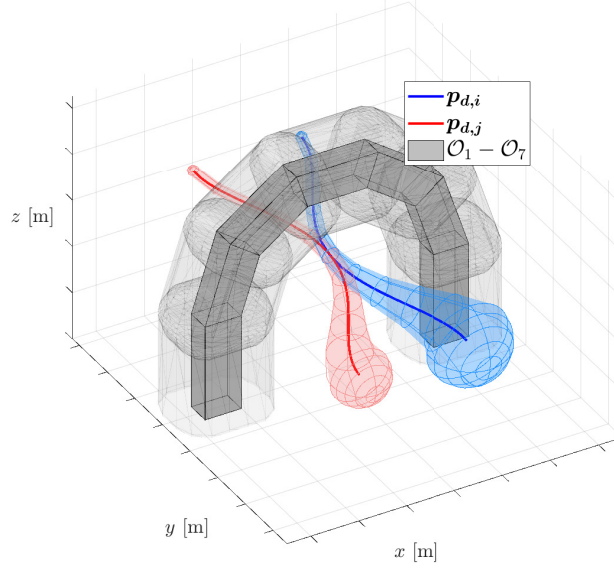
Fig. 9: Bounding tubes.

and 3 provide bounds for the individual coordination errors. For simplicity, these bounds will be expressed within this section as

$$|\xi_i(t) - \xi_j(t)| < \delta\xi_{i,j}(\|\boldsymbol{\zeta_0}\|, \|\boldsymbol{e_{p_0}}\|, \|\bar{\boldsymbol{e}}_{\boldsymbol{v}}\|, t),$$

for all the coordination strategies presented within this chapter. Henceforth, the arguments of $\delta\xi_{i,j}$ will be dropped for brevity. Moreover, the trajectories used within this thesis are uniformly continuous by construction, and thus for any $\delta p_i > 0$ there exists a $\delta\xi_{i,j} > 0$ such that for all $\xi_i, \xi_j \in [t_{d_{init}}, t_{d_{end}}]$ satisfying

$$|\xi_i - \xi_j| < \delta\xi_{i,j} \implies \|\boldsymbol{p_{d,i}}(\xi_i) - \boldsymbol{p_{d,i}}(\xi_j)\| < \delta p_i, \qquad i, j \in \mathcal{I}, \qquad i \neq j. \tag{19}$$

Therefore, for every value of $\xi_j(t) \in [t_{d_{init}}, t_{d_{end}}]$ there exists a bounded time interval where the coordination state of the ith peer lies $\xi_i(t) \in [\xi_j(t) - \delta\xi_{i,j}(t), \xi_j(t) + \delta\xi_{i,j}(t)]$. This bounded interval, the trajectory $\boldsymbol{p_{d,i}}$, and Equation (17) define a moving tube segment, illustrated in Figure 10 for times t_1 and t_2. Hence, to ensure safe separation between the coordinating agents, for every value of $\xi_j(t) \in [t_{d_{init}}, t_{d_{end}}]$ the virtual target $\boldsymbol{p_{d,j}}(\xi_j(t))$ and the tube associated with the ith coordinating peer must be sufficiently separated, as depicted in Figure 10. To this end, Equation (19) yields

$$\|\boldsymbol{p_{d,i}}(\xi_i(t)) - \boldsymbol{p_{d,j}}(\xi_j(t))\| \geq \|\boldsymbol{p_{d,i}}(\xi_j(t)) - \boldsymbol{p_{d,j}}(\xi_j(t))\| - \|\boldsymbol{p_{d,i}}(\xi_i(t)) - \boldsymbol{p_{d,i}}(\xi_j(t))\| > d_s - \delta p_i(t).$$

Then, applying the same argument as in Equation (19) to $\boldsymbol{p_{d,j}}$, choosing the least conservative bound, and plugging the result in Equation (18) yields

$$\|\boldsymbol{p_i}(t) - \boldsymbol{p_j}(t)\| > d_s - \min\{\delta p_i(t), \delta p_j(t)\} - \|\boldsymbol{e_{p,i}}(t)\| - \|\boldsymbol{e_{p,j}}(t)\|.$$

Assume that the speed-tracking precisions under nominal conditions $\bar{e}_{v,i}$ and $\bar{e}_{v,j}$ are known in the trajectory generation phase, that the gains $k_{PF,i}$ and $k_{PF,j}$ used to compute the speed command in (4) are also known in the trajectory generation phase, and that the frames for vehicles i and j are bounded by a ball of radius $r_{f,i}$ and $r_{f,j}$ centered at the center of mass of each UAS. Then, choosing

$$d_{p,i} = r_{f,i} + \frac{\bar{e}_{v,i}}{k_{PF,i}}, \qquad d_{p,j} = r_{f,j} + \frac{\bar{e}_{v,j}}{k_{PF,j}}$$

for the trajectory generation algorithm yields

$$\|\boldsymbol{p_i}(t) - \boldsymbol{p_j}(t)\| > r_{f,i} + r_{f,j} + (c_s - 1)\left(r_{f,i} + r_{f,j} + \frac{\bar{e}_{v,i}}{k_{PF,i}} + \frac{\bar{e}_{v,j}}{k_{PF,j}}\right) - \min\{\delta p_i(t), \delta p_j(t)\} - \|\boldsymbol{e_{p,i_0}}\| - \|\boldsymbol{e_{p,j_0}}\|.$$
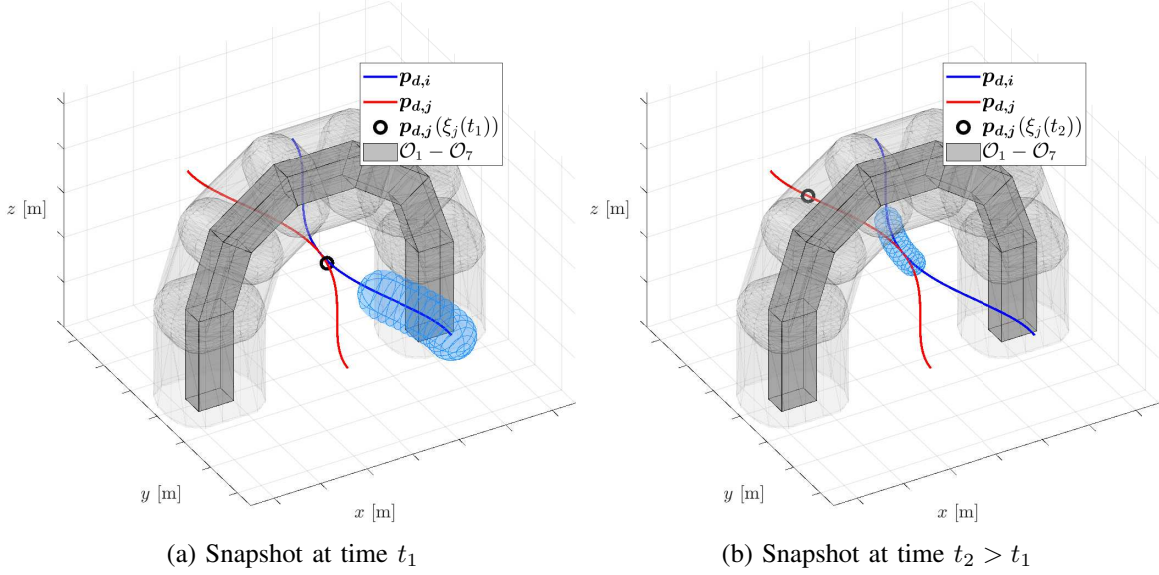
(a) Snapshot at time t_1

(b) Snapshot at time $t_2 > t_1$

Fig. 10: Trajectories, virtual target $\boldsymbol{p}_{\mathcal{T},\boldsymbol{j}}$, and tube for the ith UAS at times t_1 and t_2.

Consequently, choosing a sufficiently large c_s ensures that vehicles i and j do not collide during the mission

$$c_s \geq 1 + \frac{\sup_t \left(\min\left\{\delta p_i(t), \delta p_j(t)\right\}\right) + \|\boldsymbol{e_{p,i_o}}\| + \|\boldsymbol{e_{p,j_o}}\|}{r_{f,i} + r_{f,j} + \dfrac{\bar{e}_{v,i}}{k_{PF,i}} + \dfrac{\bar{e}_{v,j}}{k_{PF,j}}} \implies \|\boldsymbol{p_i}(t) - \boldsymbol{p_j}(t)\| > r_{f,i} + r_{f,j}.$$

In the fraction above, the numerator contains all the errors that are not modeled in the trajectory generation phase, while the denominator contains all the errors accounted in the time-critical coordination phase.

V. Technology Transitions at NASA LaRC

The Advanced Controls Research Laboratory has continuously pursued the transition of the system architecture shown in Figure 1, and the theoretical guarantees of the algorithms developed to various applications, leveraging additional funding sources for that. Among the different technology transitions accomplished in the past three years, the following efforts at NASA LaRC are of special relevance to AFOSR.

A. Online Monitoring of Coordination and Temporal Errors

Consider a human operator in charge of supervising a fleet of n UAS subject to coordination and temporal constraints. Estimating the coordination and temporal errors from the location of the vehicles, as well as the implications that these may have for the success of a mission, can be challenging for a single person. Hence, to aid human operators interpret and visualize abidance to the coordination and temporal constraints during the execution of a mission, two spider charts, shown in Figures 11 and 12, are developed.

Figure 11 presents the coordination constraints plot, which compares the coordination state of each vehicle with all its cooperating peers. This is represented in $n(n-1)$ axes that are joined at the center of the chart. Each axis represents the coordination error $\xi_i - \xi_j$ with $i \neq j$, where i can be identified by the color of the filled circular marker, and j is defined by the number at the outermost end of the axis.

For tight coordination constraints, the vehicles are tasked to drive the coordination errors to zero. This coordination goal is represented by the *zero polygon*, highlighted in black. As a result, if the marker associated with the coordination error $\xi_i - \xi_j$ lies outside the zero polygon, then the ith vehicle is ahead of the jth vehicle; whereas a marker inside the zero polygon indicates that the ith UAS is running behind when compared to the jth agent. For instance, in Figure 11 agent 1 is ahead agent 2, but perfectly coordinated with vehicle 3. Likewise, one can infer at a glance that agent 4 is behind all of its peers.
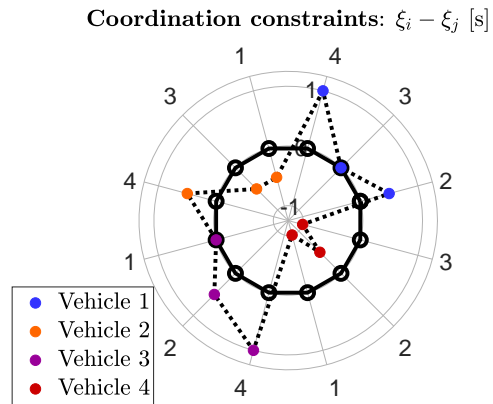
Fig. 11: Online plot for coordination errors.

Figure 12 shows the temporal constraint plots for unenforced, relaxed, and strict temporal constraints. In these charts, the coordination state of each vehicle is compared with the reference state. This is represented in n axes that are joined at the center of the chart. Each axis represents the temporal error $\xi_i - \xi_R$, where i can be identified either by the color of the marker, or the number at the outermost end of the axis. Note that the temporal goals are represented differently depending on the type of temporal constraints imposed:

1) **Unenforced**: since the vehicles are not asked to observe ξ_R, the vertices of the zero polygon are represented by empty circular markers in light gray just for reference, see Figure 12a.
2) **Relaxed**: since the temporal goal is to maintain $\xi_i - \xi_R$ within the interval $[-\Delta_t, +\Delta_t]$, an outer and an inner polygon are used to delimit the boundaries of the desired temporal window, see Figure 12b. The figure illustrates a mission with four agents and thus the inner and outer polygons are squares.
3) **Strict**: the zero polygon is highlighted in black to denote that the temporal goal is to drive all $\xi_i - \xi_R$ to zero, see Figure 12c.

(a) Unenforced

(b) Relaxed

(c) Strict
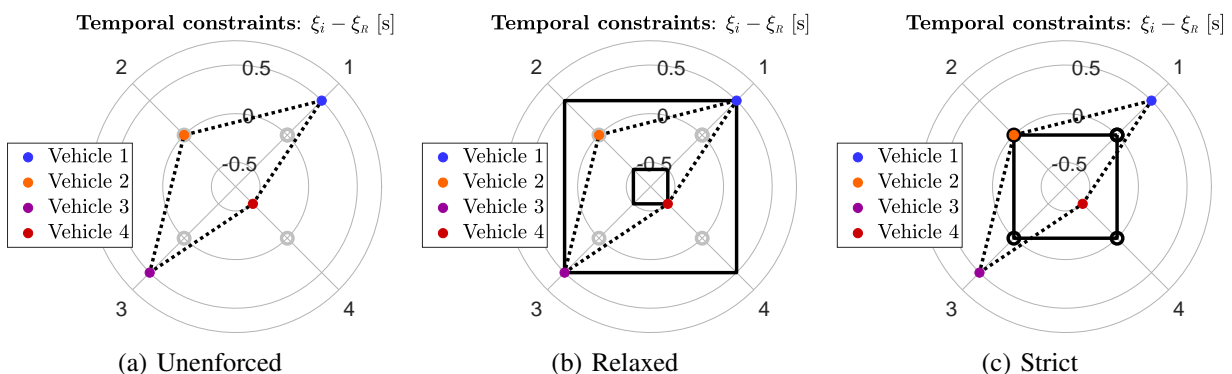
Fig. 12: Online plot for temporal errors.

B. High Fidelity 4D Simulation

This section presents simulation results for a time-critical cooperative mission through a cluttered urban-like environment with tight coordination constraints and relaxed temporal constraints. However, simulation results were developed for the six main types of time-critical coordination strategies in [17]. The results in [17] compare six simulation runs with the same mission design, initial conditions, control gains, and time-varying network topology, but different coordination and temporal constraints. Here, a group of eight UASs is tasked to converge to and follow their time-deconflicted trajectories while coordinating, to

ensure that vehicles maintain a safe separation throughout the mission. The sequential arrival of all the UASs to their final destination in the center plaza, see Figure 20, marks the completion of the mission. In this scenario, coordination is safety-critical since there are multiple narrow passages through which the UASs must pass sequentially. In fact, all vehicles must fly underneath a single arch to successfully complete the mission. Consequently, a lack of coordination in bottlenecks like this could lead to vehicle collisions. Figures 15 through 20 show snapshots of the mission, and online monitoring plots for the coordination and temporal errors at different times throughout the simulation.

The cooperating fleet is composed of eight heterogeneous multirotors: four quadcopters, two hexa-copters, and two octocopters. The underlying dynamical model for each of the UAS is based on the work developed in [18], [19], [20]. It includes non-linear translational and rotational dynamics that are coupled as follows:

$$\dot{\boldsymbol{p}_i}(t) = \boldsymbol{v_i}(t),$$
$$m_i \dot{\boldsymbol{v}_i}(t) = -f_{T,i}(t)\boldsymbol{R}_{\mathcal{B},i}^{\mathcal{I}}(t)\boldsymbol{e_3} + m_i g \boldsymbol{e_3} + \boldsymbol{f}_{D,i}(t),$$
$$\dot{\boldsymbol{R}}_{\mathcal{B},i}^{\mathcal{I}}(t) = \boldsymbol{R}_{\mathcal{B},i}^{\mathcal{I}}(t)\left(\boldsymbol{\omega}_i^{\mathcal{B}}(t)\right)^{\wedge},$$
$$\boldsymbol{J}_i\dot{\boldsymbol{\omega}}_i^{\mathcal{B}}(t) = -\boldsymbol{\omega}_i^{\mathcal{B}}(t) \times \boldsymbol{J}_i\boldsymbol{\omega}_i^{\mathcal{B}}(t) + \boldsymbol{\tau}_{T,i}^{\mathcal{B}}(t) + \boldsymbol{\tau}_{D,i}^{\mathcal{B}}(t) + \boldsymbol{\tau}_{G,i}^{\mathcal{B}}(t),$$

where the subindex $i \in \mathcal{I}$ denotes the agent identification number; $\boldsymbol{p}_i \in \mathbb{R}^3$ is the position of the center of mass of the UAS expressed in the inertial frame $\{\mathcal{I}\}$ (North-East-Down); $\boldsymbol{v}_i \in \mathbb{R}^3$ is the inertial velocity; $m_i \in \mathbb{R}$ is the mass; $f_{T,i} \in \mathbb{R}$ is the total thrust generated by the rotors; $\boldsymbol{R}_{\mathcal{B},i}^{\mathcal{I}} \in \mathbb{R}^{3\times3}$ is the rotation matrix from the body frame $\{\mathcal{B}\}$ (Forward-Right-Down) to the inertial frame $\{\mathcal{I}\}$, see Figure 13; $\boldsymbol{e_3} := [0,0,1]^{\top}$; the gravitational acceleration is $g = 9.81\,\text{m/s}^2$; $\boldsymbol{f}_{D,i} \in \mathbb{R}^3$ is the aerodynamic drag force expressed in $\{\mathcal{I}\}$; $\boldsymbol{\omega}_i^{\mathcal{B}} \in \mathbb{R}^3$ is the angular rate of the frame $\{\mathcal{B}\}$ with respect to $\{\mathcal{I}\}$ expressed in $\{\mathcal{B}\}$; $(\cdot)^{\wedge}$ denotes the hat map $\boldsymbol{J}_i \in \mathbb{R}^{3\times3}$ is the moment of inertia of the ith UAS expressed in $\{\mathcal{B}\}$; $\boldsymbol{\tau}_{T,i}^{\mathcal{B}} \in \mathbb{R}^3$ is the total torque generated by the rotors expressed in $\{\mathcal{B}\}$; $\boldsymbol{\tau}_{D,i}^{\mathcal{B}} \in \mathbb{R}^3$ is the aerodynamic drag torque expressed in $\{\mathcal{B}\}$; and $\boldsymbol{\tau}_{G,i}^{\mathcal{B}} \in \mathbb{R}^3$ is the gyroscopic torque generated by the rotation of the rotors. The model used here includes rotational and translational drag, gyroscopic effects due to the rotation of the rotors, and coriolis effects. The blade flapping model proposed in [18] is not included for the sake of simplicity.

To track the speed command generated by the cooperative path-following algorithm in Equation (4), each UAS implements a cascaded non-linear speed-tracking controller whose design leverages control strategies from [21], [22], [23], [24], [25], [26], [27], [28].

The QoS of the communication network that supports the time-critical coordination algorithms is estimated using the following expression:

$$\hat{\mu}(t) = \frac{1}{n}\frac{1}{T}\int_t^{t+T} \mathbf{Q}\mathbf{L}\left(\tau\right)\mathbf{Q}^{\top}d\tau, \quad (20)$$

with a fixed $T = 2.00\,\text{s}$. To ensure the graph $\mathcal{G}(t)$ that represents the network satisfies Assumption 5, a pseudo-random sequence of Laplacian matrices that switches every $0.50\,\text{s}$ was generated to maintain $\hat{\mu}$ within the range shown in Figure 14.

Fig. 13: Multirotor tracking the virtual target.

The simulation run includes three events that significantly perturb the individual coordination and temporal errors. These events are introduced intentionally to evaluate how the time-critical coordination
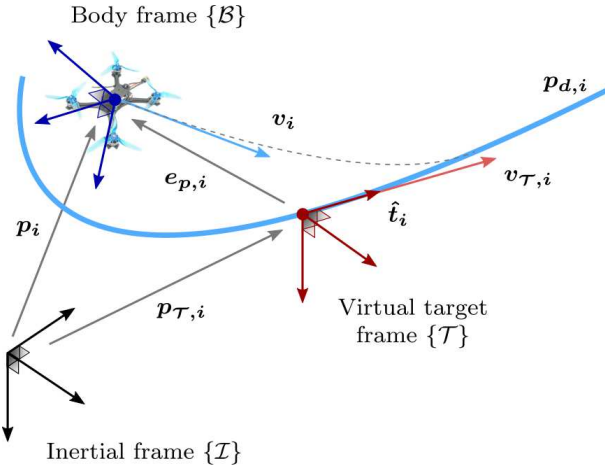
and path-following algorithms perform under realistic disturbances. The following list describes the nature and timing of these disturbances, as well as the effects on the cooperating fleet:

1) **Initial position error**: the cooperative path-following algorithm is engaged at $t = 5\,\text{s}$. At that time, the actual positions of the UASs present an offset with respect to the desired positions on the trajectory. This can also be observed in the norm of the position error, shown in Figure 21. Figure 15 shows a snapshot of the mission shortly after the cooperative path-following algorithm is engaged. In this figure the vehicles are already tilted towards the desired position in an attempt to converge to the path. Note also that the initial position error has propagated through the coordination dynamics, leading to coordination and temporal errors in all simulation runs. Figure 16 illustrates how, after some time, the path-following algorithm makes the vehicles converge to their virtual targets. Simultaneously, the time-critical coordination algorithm synchronizes the virtual targets and enforces the desired temporal constraints. Three relevant symbols are visible in the 3D plot in Figures 15 and 16:

   - an empty circular marker $\bigcirc$ denotes the position of the virtual target $\boldsymbol{p}_{\mathcal{T},i}(t) = \boldsymbol{p}_{d,i}(\xi_i(t))$;
   - a filled star $\bigstar$ represents the desired position given by the planned trajectory $\boldsymbol{p}_{d,i}(\xi_{R}(t))$;
   - and two $\times$ symbols are used to delimit the trajectory segment that meets the relaxed temporal constraints at time t. Therefore, the trailing and leading $\times$ markers are located at $\boldsymbol{p}_{d,i}(\xi_{R}(t) - \Delta_t(t))$ and $\boldsymbol{p}_{d,i}(\xi_{R}(t) + \Delta_t(t))$, respectively.

2) **Wind gust engaged**: a rectangular pulse with a magnitude of $8\,m/s$ is used to simulate a sudden wind gust. As depicted in Figure 28, the wind is engaged at $t = 20\,\text{s}$. This disturbance is applied to all the UASs at the same time. However, the individual vehicle responses to the wind vary since the fleet is heterogeneous. Figure 17 shows a snapshot of the mission shortly after the wind gust is engaged. The arrows that appear next to each UAS icon denote the wind direction, which coincides with the direction of the drag force that pulls from each of the vehicles. This disturbance creates a position error that is clearly visible in Figure 21. As a result, Figure 17 shows an increase in the coordination and temporal errors. Notice that the overall effect of this wind gust is to push the fleet further behind the planned schedule. This can be inferred from the comparison of the temporal errors in Figures 16 and 17, or simply by looking at Figure 25. Note that while the wind is engaged the vehicles have difficulty tracking the virtual target and speed command with the same precision as with no wind, see Figures 21 and 22. However, as the speed-tracking controller of each UAS learns to compensate for the wind, the position errors converge to a relatively small neighborhood of the origin. As a result, Figure 18 shows how the coordination errors return to a reasonably small neighborhood of the zero polygon, as expected for tight coordination constraints. Note also that in Figure 18 the temporal errors remain within the desired temporal window.

3) **Wind gust disengaged**: the sudden removal of the wind gust at $t = 80\,\text{s}$ causes the speed-tracking controller of every vehicle to overcompensate for a non-existent disturbance. As a result, the UASs overshoot their virtual targets, incurring in a position error shown in Figure 21. Figure 19 provides
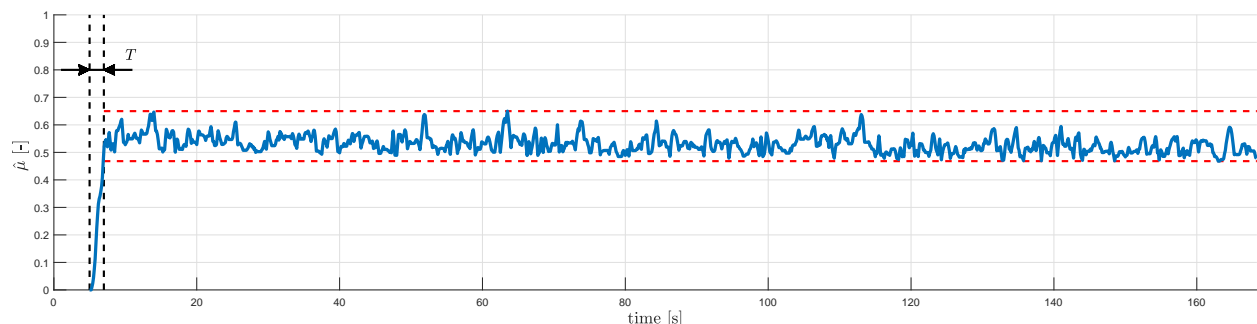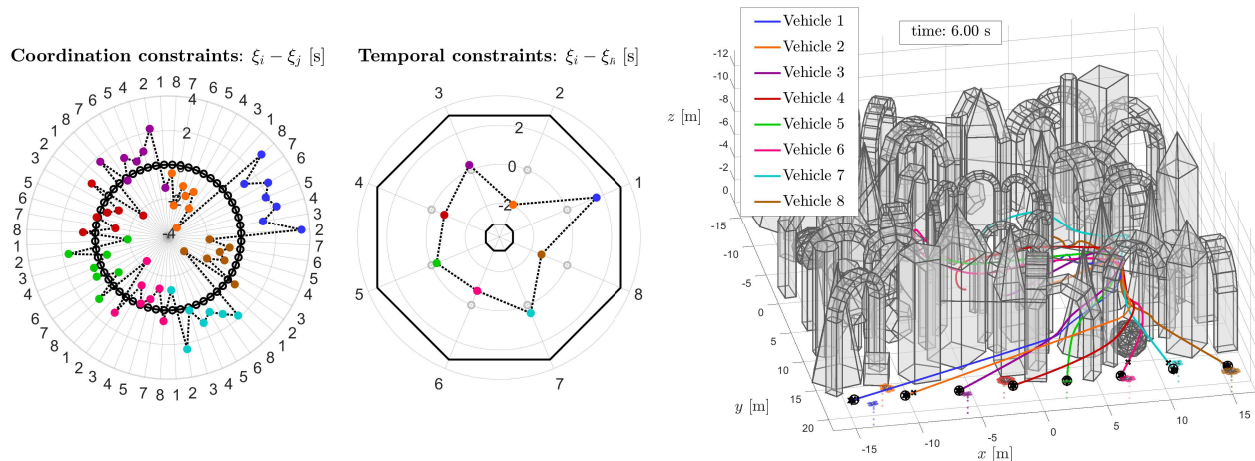

Fig. 14: QoS of the communication network.

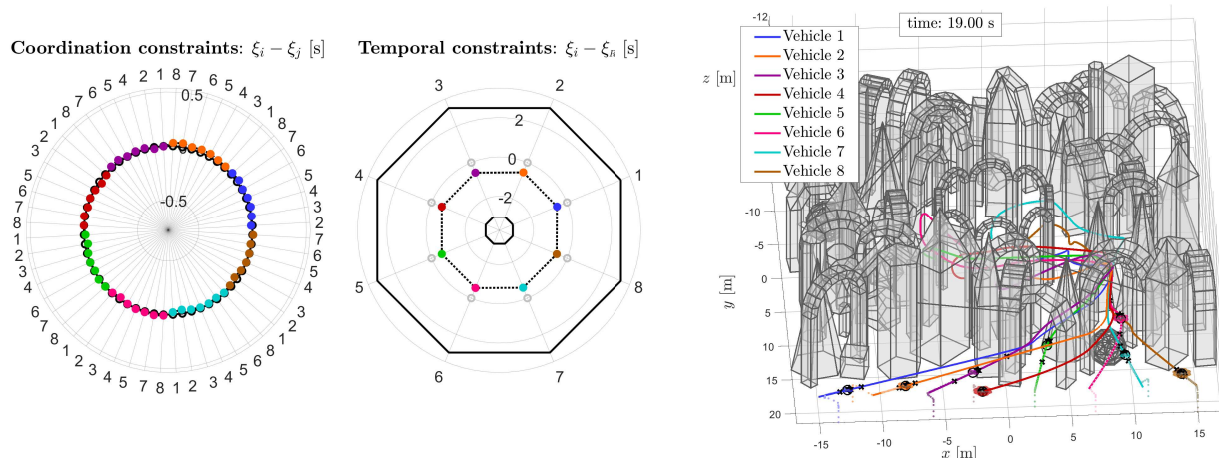Fig. 15: Simulation results 1 s after the time-critical coordination algorithm is engaged.

Fig. 16: Simulation results 1 s before the wind gust is engaged.

a snapshot of the mission shortly after the wind gust is removed. Again, the position error has propagated through the coordination dynamics, leading to an increase in the coordination errors. As for the temporal error, the overall effect of this disturbance is to advance the fleet forward along the mission, see Figure 25. After some time, the speed-tracking controllers learn that the wind has ceased. Then, the path-following algorithms are able to reduce the position errors. The time-critical coordination algorithm cancels out the effects of this disturbance on the coordination errors, which converge to a small neighborhood of the zero polygon, as shown in Figure 20.

Figure 24 shows the coordination errors, which converge to a neighborhood of the origin as anticipated in Theorem 2. Figure 25 shows the temporal errors. Note the effects of engaging and disengaging the wind gust at $t = 20$ s and $t = 80$ s, respectively. As predicted in Theorem 2, the temporal error drifts linearly until the link peers reach the boundary of the temporal window, see Figure 25 between $t = 90$ s and $t = 130$ s. During that time the switched system is in mode $\varnothing$. Then, the link weights $\omega_{R_i}(t)$ switch persistently between 0 and 1 to prevent the drift of the temporal errors. Consequently, the system alternates between modes $\varnothing$ and $\bigcirc$, ensuring that all temporal errors remain within a neighborhood of the temporal window, as anticipated in Corollary 2. Notice that the temporal window is set to a constant value $\Delta_t(t) \equiv 3$ s.

Figure 26 shows the integral states of the end peers. Note that the integral states do not exactly learn
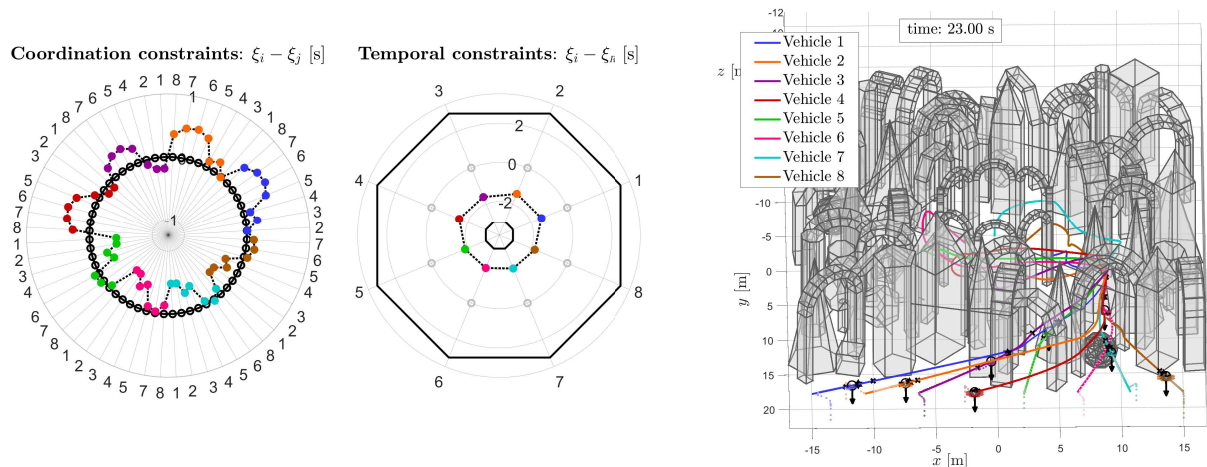
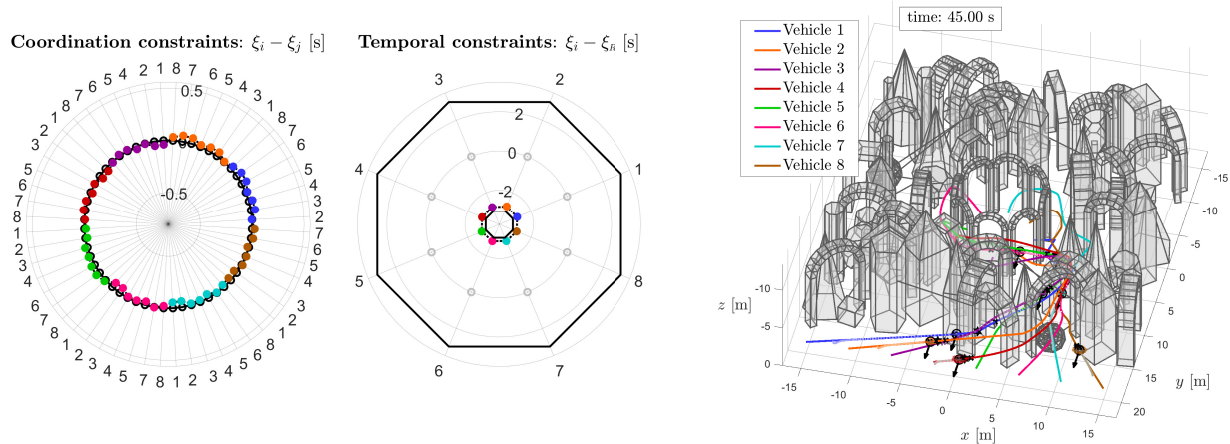Fig. 17: Simulation results 3 s after the wind gust is engaged.

Fig. 18: Simulation results 25 s after the wind gust is engaged.

the mission rate when the system is in mode $\emptyset$, see Figure 26 between $t = 90\,\mathrm{s}$ and $t = 130\,\mathrm{s}$. However, when the link peers reach the boundary of the temporal window the end peers are forced to persistently correct their integral states as the the weights $\omega_{R_i}(t)$ are set to 1.

Figure 27 shows the norm of the desired velocity as computed during the trajectory generation phase, the norm of the velocity command, and the norm of the actual vehicle velocity. There is a noticeable lag between the desired velocity and the velocity command. This is expected and caused by the delays in the progress of the mission, which are bounded for relaxed temporal constraints.

Figure 23 shows the temporal evolution of the distance among the centers of mass of the cooperating agents. Note that the distance among vehicles is always greater than $0.50\,\mathrm{m}$, which was established as the safe separation threshold and is marked by a dashed red line.
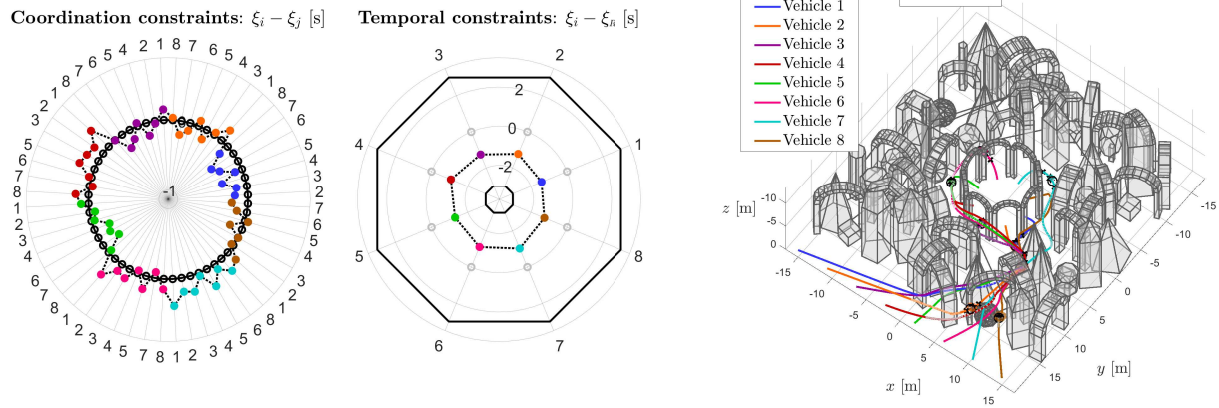
Fig. 19: Simulation results $3\,\mathrm{s}$ after the wind gust is disengaged.
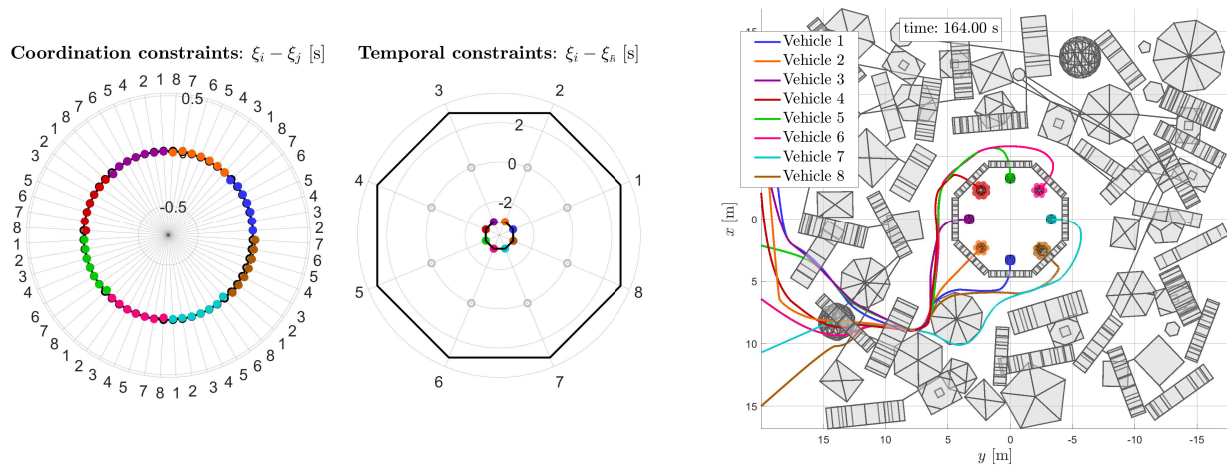
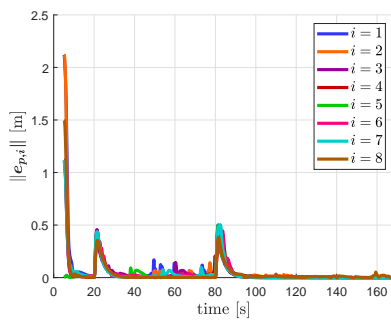Fig. 20: Results at the conclusion of the simulation.
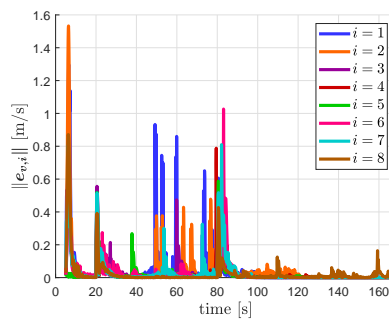

Fig. 21: Position error.
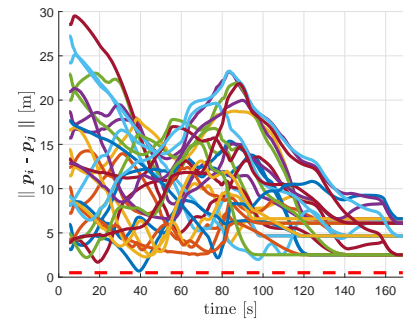

Fig. 22: Speed error.

Fig. 23: Separation distance.

REFERENCES

[1] A. Gahlawat, P. Zhao, A. Patterson, N. Hovakimyan, and E. Theodorou, "$\mathcal{L}_1$-$\mathcal{GP}$: $\mathcal{L}_1$ adaptive control with Bayesian learning," in *Proceedings of the 2nd Annual Conference on Learning for Dynamics and Control (L4DC)*, vol. 120, Online, 2020, pp. 1–12.
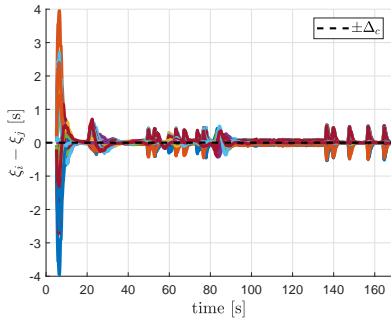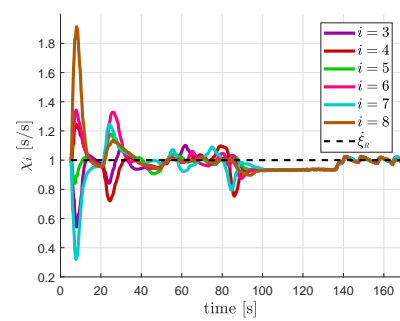
Fig. 24: Coordination error.
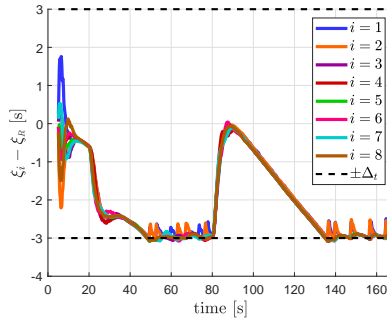
Fig. 25: Temporal error.

Fig. 26: Integral states.

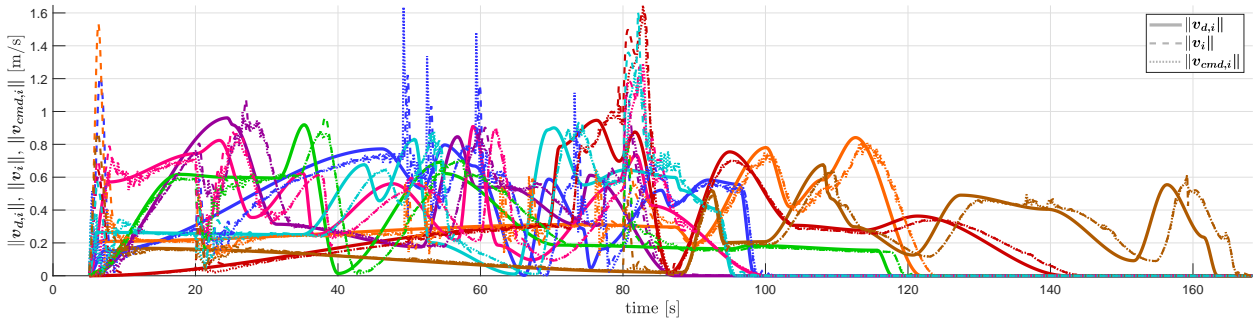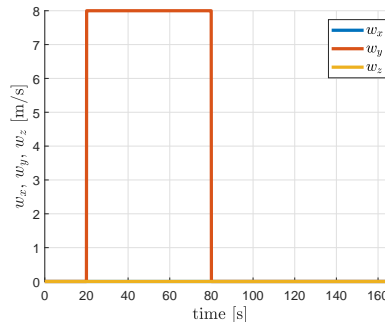
Fig. 27: Speed profiles.

Fig. 28: Wind.

[2] A. Lakshmanan, A. Gahlawat, and N. Hovakimyan, "Safe feedback motion planning: A contraction theory and $\mathcal{L}_1$-adaptive control based approach," *arXiv:2004.01142*, 2020, Accepted for publication in the 59th IEEE Conference on Decision and Control.

[3] A. Gahlawat, A. Lakshmanan, L. Song, A. Patterson, Z. Wu, N. Hovakimyan, and E. A. Theodorou, "Contraction $\mathcal{L}_1$-adaptive control using Gaussian processes," in *Learning for Dynamics and Control (L4DC)*. PMLR, 2021, pp. 1027–1040.

[4] Y. Cheng, P. Zhao, M. Gandhi, B. Li, E. Theodorou, and N. Hovakimyan, "Robustifying reinforcement learning policies with $\mathcal{L}_1$ adaptive control," *arXiv preprint arXiv:2106.02249*, 2021.

[5] P. Zhao, Y. Mao, C. Tao, N. Hovakimyan, and X. Wang, "Adaptive robust quadratic programs using control Lyapunov and barrier functions," in *2020 59th IEEE Conference on Decision and Control (CDC)*. IEEE, 2020, pp. 3353–3358.

[6] N. Wan, A. Gahlawat, N. Hovakimyan, E. A. Theodorou, and P. G. Voulgaris, "Cooperative path integral control for stochastic multi-agent systems," *arXiv preprint arXiv:2009.14775, to appear in American Control Conference (ACC), 2021*, 2020.

[7] ——, "Distributed algorithms for linearly-solvable optimal control in networked multi-agent systems," *arXiv preprint arXiv:2102.09104*, 2021.

[8] L. Song, N. Wan, A. Gahlawat, N. Hovakimyan, and E. A. Theodorou, "Compositionality of linearly solvable optimal control in networked multi-agent systems," *arXiv preprint arXiv:2009.13609, to appear in American Control Conference (ACC), 2021*, 2020.

[9] E. Xargay, "Time-critical cooperative path-following control of multiple unmanned aerial vehicles," Ph.D. dissertation,

University of Illinois at Urbana-Champaign, Urbana, IL, USA, 2013.

[10] V. Cichella, R. Choe, S. B. Mehdi, E. Xargay, N. Hovakimyan, V. Dobrokhodov, I. Kaminer, A. M. Pascoal, and A. P. Aguiar, "Safe coordinated maneuvering of teams of multirotor unmanned aerial vehicles: A cooperative control framework for multivehicle, time-critical missions," *IEEE Control Systems Magazine*, vol. 36, no. 4, pp. 59–82, August 2016.

[11] J. A. Winnefeld, Jr., and F. Kendall, "Unmanned systems integrated roadmap, 2013-2038," Department of Defense, Tech. Rep. 14-S-0553, 2013.

[12] K. M. Fahey and M. J. Miller, "Unmanned systems integrated roadmap, 2017-2042," Department of Defense, Tech. Rep., 2017.

[13] I. Kaminer, A. Pascoal, E. Xargay, N. Hovakimyan, V. Cichella, and V. Dobrokhodov, *Time-Critical Cooperative Control of Autonomous Air Vehicles*.   Cambridge, MA: Elsevier, 2017.

[14] J. Puig-Navarro, E. Xargay, R. Choe, and N. Hovakimyan, "Time-critical coordination of multiple UAVs with absolute temporal constraints," in *AIAA Guidance, Navigation and Control Conference*, Kissimmee, FL, January 2015, AIAA 2015-0595.

[15] J. Puig-Navarro, N. Hovakimyan, and B. D. Allen, "Time-coordination strategies and control laws for multi-agent unmanned systems," in *AIAA Aviation Technology, Integration, and Operations Conference*, Denver, CO, June 2017, AIAA 2017-3990.

[16] V. Cichella, "Cooperative autonomous systems: Motion planning and coordinated tracking control for multi-vehicle missions," Ph.D. dissertation, University of Illinois at Urbana-Champaign, Urbana, IL, USA, 2018.

[17] J. Puig-Navarro, "Distributed time-critical coordination strategies for unmanned aerial systems in cluttered environments," Ph.D. dissertation, University of Illinois at Urbana-Champaign, Urbana, IL, USA, June 2020.

[18] J. W. Vervoorst, "A modular simulation environment for the improved dynamic simulation of multirotor unmanned aerial vehicles," Master's thesis, University of Illinois at Urbana-Champaign, Urbana, IL, USA, 2016.

[19] V. Stepanyan, K. S. Krishnakumar, and A. Bencomo, "Identification and reconfigurable control of impaired multi-rotor drones," in *AIAA Guidance, Navigation and Control Conference*, San Diego, CA, USA, January 2016, pp. 1–20, aIAA 2016-1384.

[20] V. Stepanyan and K. S. Krishnakumar, "Estimation, navigation and control of multi-rotor drones in an urban wind field," in *AIAA Information Systems*, Grapevine, TX, USA, January 2017, pp. 1–26, aIAA 2017-0670.

[21] T. Lee, M. Leok, and N. H. McClamroch, "Geometric tracking control of a quadrotor UAV on SE(3)," in *IEEE Conference on Decision and Control*, Atlanta, GA, USA, December 2010, pp. 5420–5425.

[22] T. Lee, "Geometric tracking control of the attitude dynamics of a rigid body on SO(3)," in *American Control Conference*, San Francisco, CA, USA, June 2011, pp. 1200–1205.

[23] ——, "Robust global exponential attitude tracking controls on SO(3)," in *American Control Conference*, Washington, DC, USA, June 2013, pp. 2103–2108.

[24] ——, "Global exponential attitude tracking controls on so(3)," *IEEE Transactions on Automatic Control*, vol. 60, no. 10, pp. 2837–2842, February 2015.

[25] J. Wang, I. A. Kapitaniuk, S. A. Chepinskiy, D. Liu, and A. J. Krasnov, "Geometric path following control in a moving frame," *IFAC-PapersOnLine*, vol. 48, no. 11, pp. 150–155, September 2015.

[26] S. Kulumani and T. Lee, "Constrained geometric attitude control on SO(3)," *International Journal of Control, Automation and Systems*, vol. 15, no. 6, pp. 2796–2809, December 2017.

[27] Y. Zhu, X. Chen, and C. Li, "Some discussions about the error functions on SO(3) and SE(3) for the guidance of a UAV using the screw algebra theory," *Advances in Mathematical Physics*, vol. 2017, pp. 1–11, January 2017.

[28] K. A. Ackerman, I. M. Gregory, and N. Hovakimyan, "Flight control methods for multirotor UAS," in *International Conference on Unmanned Aircraft Systems (ICUAS)*, Washington, DC, USA, June 2019, pp. 353–361.

VI. Disclaimer

The views and conclusions contained herein are those of the author and should not be interpreted as necessarily representing the official policies or endorsements, either expressed or implied, of the AFOSR or the U.S. Government.

VII. Personnel Partially Supported by the Grant

1) Naira Hovakimyan, Professor
2) Aditya Gahlawat, Postdoctoral Research Associate
3) Pan Zhao, Postdoctoral Research Associate
4) Neng Wan, Graduate Research Assistant

VIII. Honors and Awards

- 2019 AIAA Pendray Aerospace Literature Award
- 2018 IEEE Fellow
- Numerous invited talks, plenaries, distinguished seminars.

IX. NASA Points of Contact

- Irene Gregory (Irene.M.Gregory@nasa.gov)
- Danette Allen (danette.allen@nasa.gov)